Coupled estimation of incoherent ~~inertia gravity wave field~~ internal tide and turbulent ~~balanced~~ motions via statistical modal decomposition

Igor Maingonnat[1], Gilles Tissot[1,*], and Noé Lahaye[1,*]

[1]INRIA Rennes Bretagne Atlantique, IRMAR – UMR CNRS 6625, av. General Leclerc, 35042 Rennes, France
[*]These authors contributed equally to this work.

Correspondence: Igor Maingonnat (igor.maingonnat@inria.fr)

Abstract. ~~The~~ We present a data-driven modal decomposition method that extracts the part of an incoherent internal tidal wave that correlates with the proper orthogonal decomposition ~~modes of the balanced motion. Using the rotating shallow water as a canonical model for wave / balanced flowinteractions, we describe the connection between the variability of the jet and the incoherence of the internal wave, which provides some theoretical foundations to the proposed method . This expected connection is then confirmed by numerical simulations of the rotating shallow water model, and the variability modes of the jet and wave field are analysed. Finally, an algorithm for estimating the jet component and the associated wave field from single snapshots of the sea level height is proposed and tested using outputs from numerical simulations. We show that such algorithmprovides a valuable coupled estimate of the two dynamics, especially in configurations where the~~ (POD) of a turbulent mesoscale flow. This method exploits the *a priori* knowledge that the incoherent internal tide arises from interactions between an incident wave and the turbulent flow, and exploits the corresponding statistical correlation between the two types of motions. The method is presented and tested in an idealised framework based on the Rotating Shallow Water model, where we provide a physical interpretation for the decomposition method based on theoretical considerations. Using idealised simulations with a plane wave propagating through a zonal turbulent jet, we first propose the use of the modal decomposition method as a data analysis technique to understand how the wave is scattered by the flow. In a second step, we construct an estimation algorithm capable of separating the entangled contributions of the wave ~~signal is small compared to the jet .~~ and mesoscale motions from a single sea surface height snapshot. This algorithm, which consists of estimating the POD coefficients of the turbulent flow – shared by the wave and jet modes – is particularly suitable for configurations where the jet contribution to the SSH is larger than that of the wave.

Keywords: Internal ~~wave interactions, wave~~ tide scattering, data-driven methods, estimation.

1 Introduction

Internal tides (IT) are internal waves generated by ~~interactions between the barotropic tide and topographic features~~the interaction of the barotropic tide with the irregular topography, such as ridges or continental slopes, ~~and~~ that propagate mainly at tidal frequencies. They are ubiquitous in the ocean, and play a crucial role in vertical mixing and energy transport, especially in

the deep ocean (**??**). Propagating over large distances, they encounter regions with energetic mesoscale turbulence, and ~~lose~~ loose their fixed phase relationship with the astronomical forcing through ~~the nonlinear~~ non-linear interactions with this turbulence. The resulting incoherent internal tide field (often called ~~"~~"non phase-locked~~" or "~~" or "non-stationary~~" ~~"~~ internal tide in the literature), highly unpredictable, complicates for example our ability to disentangle internal tides and low-frequency turbulent signals from satellite data (**?**). ~~**??** show that for the principal semidiurnal tide (M2) the incoherent part accounts for approximately half of the IT variance (44% in **?**), averaged over the global ocean . There is therefore~~ Due to their large coverage and overall impact on the ocean (**??**), there is a need to ~~better~~ understand how incoherent waves propagate, ~~and to develop algorithms that could estimate and separate the surface signatures of the two dynamics in~~ which includes developing algorithms for estimating and separating the surface signature of internal tides and the mesoscale flow from observational data.

In the ~~oceanographic~~ physical oceanography community, various studies have examined the impact of a ~~balanced (turbulent) jet on the inertia-gravity wave field properties in both realistic and idealised models. For instance, **?** demonstrated on realistic simulations~~ low frequency turbulent flow on internal waves, using various methodological approaches. **?** demonstrated, using idealized numerical experiments featuring a plane wave propagating through a zonal baroclinic jet, that the increase of energy of ~~a fully turbulent jet contribute significantly to~~ the turbulent jet enhances the loss of coherence of the ~~wave field. **??** used geometric wave theory to examine internal tide reflections and refractions by the Gulf Stream in both realistic and idealised simulations, assessing the influence of the IT's propagation angle with the jet on waves deflections. **?** focused on the statistical properties of an internal tide scattered by a random flow from idealised simulation, where a kinetic transport equation is derived to study the wave energy propagation through a random media.~~ internal tide field. **?** described, based on kinetic transport theory, how random quasigeostrophic and barotropic flows impact energy exchanges in a scattered plane wave. ~~In the range of modal decomposition technique, **???**and more other studied the feasibility to study the~~ **???**, among others, studied the propagation of IT ~~on~~ using reduced order models ~~based on vertical mode projection , adapted to express the vertical structure of IT. **?** studied the~~ derived from a Galerkin projection onto a basis of vertical modes. **?** applied a multiscale analysis in the rotating shallow water model (RSW) to study the scattering of inertia-gravity waves (IGW) by ~~decomposing the non-linear interactions terms of a rotating shallow water (RSW) model on a normal mode decomposition, and using the theory of resonant triad. They~~ the low-frequency flow. The authors showed that waves that resonantly interact with the jet transfer their energy to waves of equal wavelength, and that this transfer is intensified for short-wavelength and strong ~~background~~ turbulent flows.

~~In this paper, we consider a data-driven approach to extract and analyse the wave field scattered by a balanced turbulent jet in a numerical simulation. Amongst the numerous data-driven decomposition techniques in fluid mechanics to extract meaningful physical quantities, we focus on methods based on the proper orthogonal decomposition (POD) (**??**). The POD (often called empirical orthogonal functions – EOF – in the geophysical fluid dynamics community) is a modal decomposition method to extract recurrent phenomena, namely coherent structures, in flow data (**?**). Its frequency-domain variant, the spectral proper orthogonal decomposition (**??**), provides a decomposition which is optimal to capture the variance associated with realisations of~~ A consequence of the non-linear interactions between the IT and the low-frequency flow is a spectral broadening, often referred to as "cusps" (**??**), which is a direct translation of the loss of coherence of the signal. Indeed, the ~~Fourier spectrum. The method we propose, to examine wave scattering by turbulence, is based on the analysis of the complex wave amplitudes,~~

extracted by complex demodulation, which is slowly varying (compared to the typical wave period) due to interactions with a fluctuating jet. We investigate the scattering by extracting the correlations between the slow modulations of the quadratic non-linear term becomes, in time frequency-space, a convolution operator between the wave and the coherent structure of the jet by applying the extended POD method (EPOD; **?**). Prior to this, we introduce the broadband POD method (BBPOD) to extract the most energetic modes of the broadband wave field, allowing for a comparison of the two decomposition methods. As it will be described, BBPOD can be viewed as a reformulation of SPOD, introducing explicitly the filtering frequency band, allowing us to interpret correctly the modes associated with the scattered field, due to spectral broadening. For the sake of clarity in what follows, we will avoid using the term "coherent structures" of the (incoherent)wave field, and prefer the term optimal modes or simply modes of the wave, as the term "incoherent" have a different meaning here. mesoscale fluctuations. The spectrum of coherent IT, which corresponds to a finite Dirac sum, is thus broadened by the mesoscale flow, giving rise to an incoherent broadband spectrum. Spectral broadening is a general characteristic of scattered wave fields, widely studied in other disciplines (*e.g.* in aeroacoustics, **??**).

Based on the proposed decomposition method, we also address the issue of the estimation and separation of the internal tide and the mesoscale flow from observations. The development of algorithms has also recently received a great attention in the literature. Recently, several methodological approaches have been developed to address the issue of separation of IT and Balanced Motions (BM), motivated in particular by the launch of the SWOT mission (**?**). Due to the presence of an incoherent component, to similar wavelengths and the strong aliasing in time between two swaths, simple filtering or harmonic decomposition strategies are often inefficient. Some methods are based on physical approaches, such as in **?**, who assumed a weak signature of IT on surface density fields , and consider and considered potential vorticity dynamics to identify the balanced motion (BM) BM from the observations. As for more complex In the realm of data-assimilation techniquesmethods, **?** developed a coupled iterative approach based on a 4D-Var assimilation for the algorithm for IT and back-and-forth nudging for the BM. In the range of data-driven methods, there is has been a recent focus on deep-learning approaches to disentangle low and high frequency signal (**??**). **?** address in particular the difficulty caused by the long revisit time of altimeters by developing a method based on single SSH snapshots. **?** developed a method In closer connection to the methodology that will be presented in this paper, **?** and **?** proposed methods based on a decomposition of IT onto spectral EOF, in order to map satellite observations to a realistic model, and estimate the Proper Orthogonal Decomposition (POD) of the IT sea surface height (SSH) contribution of the internal tide. Here, we propose a similar methodology to the previous two , which aims at performing an additional step, taking advantage of the EPOD technique to have a complete estimate of the jet field, computed from HYCOM-based realistic simulation in the former, and filtered daily SWOT swath in the latter.

In this paper, we introduce a data-driven modal decomposition of a wave field scattered by a turbulent mesoscale jet. We focus on methods based on the POD (**??**). The POD (often called empirical orthogonal functions – EOF – in the geophysical fluid dynamics community) is a modal decomposition method designed to extract recurrent phenomena from flow data (**?**). We propose two different methods, namely the brodband POD (BBPOD) and an algorithm based on the extended POD (EPOD; **?**). Both methods rely on the physical consideration that the scattering of the wave field, corresponding to time-evolution of its complex amplitude, are driven by the mesoscale dynamics and therefore occurs at a similar timescale (**?**). With this

consideration in mind, the BBPOD algorithm corresponds to a POD of the complex demodulated variables, and extracts the most energetic modes of variability of a high frequency component associated with a broadband spectrum. It share similarities with the spectral POD algorithm (**??**), as will be further discussed in the manuscript. The second method applies the extended POD method to the complex wave amplitude in order to extract spatial modes that are correlated with the POD modes of the jet, thereby providing a decomposition of the flow that takes into account the coupling between the mesoscale dynamics and the wave~~, including estimates of velocities,~~ .

Then, we take advantage of this EPOD-based decomposition method to build an algorithm for estimating the mesoscale and wave fields – including velocities – from a single SSH observation. In particular, we address configurations where the jet component dominates the flow, in which case the weak internal ~~wave~~ tide signal can still be estimated by the coupling induced by their correlation. The algorithm is tested on ~~an idealised simulation of the~~ idealised simulations of a one layer RSW model representing such ~~a~~ configuration.

The plan of this paper is as follows. We begin in Sect. **??** by describing the ~~model used to investigate the dynamics of a wave field interacting with a zonal turbulent flow~~RSW model on which is based this study. Derivation of equations for the ansatz of the complex amplitudes are then given in order to complement the data-driven methods with a physical interpretation. In Sect. **??**, the ~~different methods are introduced, namely the BBPOD~~ BBPOD and EPOD-based methods are first presented (Sect.~~**??**) and the EPOD (Sect.**??**). The~~ **??** and **??**), before describing the algorithm to disentangle observations ~~is presented in Sect.**??**. Section **??** presents~~ (Sect. **??**). Finally, Sect. **??** gathers the numerical results computed from ~~idealised simulations. The~~ five idealised simulations, including a data analysis of the variability of the wave field ~~is examined in Sect.**??**, by means of the modal decomposition techniques of this study. Thereafter,~~ (Sect. **??**), and results of estimates of the ~~two dynamics are given in Sect.**??**.~~ mesoscale jet and the internal tide (Sect. **??**).

2 ~~Non linear wave-flow~~ Non-linear interactions between mesoscale turbulence and high frequency waves

~~This section begins by presenting the RSW model used to investigate incoherent waves interacting with a turbulent flow. Thereafter, we derive a simple equation for the incoherent complex wave amplitudes and we introduce some motivations of the method that will be presented in Sect. **??**.~~ We present in this section the (dimensionless) one-layer Rotating Shallow Water model (RSW), which is an adequate idealistic model to analyze non-linear interactions between high-frequency waves and a low frequency turbulent flow (*e.g.* **??**). A set of asymptotic equations is then derived for the the complex wave amplitude and the evolution of the incoherent part. We shall mention that, since internal tides interacting with mesoscale turbulence are the main target of this study, the waves will be often reffered to as internal tide (IT) and the low-frequency turbulent flow as mesoscale flow throughout the paper.

2.1 ~~One layer rotating shallow water model~~

2.1 One-layer rotating shallow water model

~~To examine the propagation of internal tides through a nearly-balanced jet, we study the solutions of the one layer rotating shallow water (RSW) model, which is minimal to represent wave-jet interactions (*e.g.* **??**). The~~ For this specific analysis, the RSW equations are non-dimensionalized as follows.

$$t^\sharp = f_0^{-1} t;\ (x^\sharp, y^\sharp) = (l\,x, l\,y);\ \boldsymbol{v}^\sharp = (u^\sharp, v^\sharp) = (U\,u, U\,v);\ h^\sharp = H_o \frac{R_o}{B_u} h,$$

where the superscript $.^\sharp$ refers to the dimensional variables. The parameter f_0 is the Coriolis frequency, $\boldsymbol{v}$ is the horizontal velocity and h is the SSH, with a layer thickness at rest H_o. The dimensionless parameters are the Rossby number $R_o = U/f_0 l$ and the Burger number $B_u = R_d^2/l^2$, where $R_d = \frac{\sqrt{g H_0}}{f_0}$ is the Rossby deformation radius. The characteristic timescale is taken here as the inertial time $T = f_0^{-1}$, ~~adapted for studying internal wave propagation ,~~ which is well suited for studying IT propagation as it is the lower frequency bound of the internal wave spectrum. The reference length scale l and the reference ~~speed~~ current U are chosen to be of the ~~order of the~~ typical jet thickness and ~~speed~~velocity, respectively. ~~Moreover, the~~ The Coriolis frequency follows the beta-plane approximation, which writes ~~in its dimensionless form~~(in dimensionless form) $f(y) = 1 + \beta y$, where $\beta = R_d/(R_T\sqrt{B_u})$, with R_T the Earth radius. Including the β-term is necessary to ~~obtain~~ maintain a zonal jet ~~and to study the scattering of the wave in a small domain (?). An~~ structure (**?**). Finally, we consider a monochromatic wave forcing term ~~$\boldsymbol{q}_{frc,\omega} = (h_{frc,\omega}, \boldsymbol{v}_{frc,\omega})^T$, which is kept under a general form in this section, is also added on the right hand-side of the equations.~~ $\boldsymbol{q}_{frc,\omega} = (f_{h,\omega}, \boldsymbol{f}_{\boldsymbol{v},\omega})^T = \Re(\tilde{\boldsymbol{f}}_{\boldsymbol{q},\omega}(x,y)e^{i\omega t})$ (which will be specified in Sect. **??**).

Introducing this non-dimensionalisation into the RSW model leads to the following set of equations, defined on ~~$\Omega \times \mathbb{R}_+$ with $\Omega \subset \mathbb{R}^2$ bounded:~~ $\mathbb{R}^+ \times \Omega$ where $\Omega \subset \mathbb{R}^2$ is the bounded spatial domain:

$$\partial_t h + B_u \mathrm{div}(\boldsymbol{v}) = -R_o\left[(\boldsymbol{v}\cdot\nabla)h + h\ \mathrm{div}(\boldsymbol{v})\right] + h_{frc,\omega} f_{h,\omega} \tag{1a}$$

$$\partial_t \boldsymbol{v} + (1+\beta y)\boldsymbol{v}^\perp + \nabla h = -R_o(\boldsymbol{v}\cdot\nabla)\boldsymbol{v} + {}_{frc,\omega}\boldsymbol{f}_{\boldsymbol{v},\omega} \tag{1b}$$

where $\boldsymbol{v}^\perp = (-v, u)^T$. In the numerical tests, periodic boundary conditions will be considered, and inhomogeneities in the y direction will be treated using sponge layers (details given in Sect. **??**). It can be noted that periodic domains are compatible with the bounded domain hypothesis.

2.2 Complex wave amplitude ansatz

~~The inertia-gravity wave~~

The total wave field $\boldsymbol{q}_\omega = (u_\omega, v_\omega, h_\omega)^T$ is expressed as:

$$\boldsymbol{q}_\omega(t) = \Re(\tilde{\boldsymbol{q}}_\omega(t)e^{i\omega t}), \tag{2}$$

where $\tilde{\boldsymbol{q}}_\omega(t)$ is the complex wave amplitude vector, and ω the dominant wave frequency (the same as in the forcing term). It is assumed that the complex wave amplitude is slowly varying (in time), which reflects that the wave is scattered by the low-frequency mesoscale flow, *i.e.* we assume scale separation (in time) between the mesoscale flow and the IT (see Sect. **??**). This ansatz is ~~represented here with a slowly time-varying wave ansatz, which is adequate for representing an IGW propagating~~

through the slowly varying jet responsible of the coherence loss.This assumption is borrowed from high-frequency asymptotic approximations methods, such as ray tracing or WKB methods (*c.f.* **?**). Here, only a time scale separation between the jet and the wave is assumed in order to extract the two components by filtering. The total wave field $\boldsymbol{q}_\omega = (u_\omega, v_\omega, h_\omega)^T$ is thus expressed as: , and also corresponds to the dominant term of a scattered wave in standard multiscale analysis (*e.g.* **??**, in the framework of the RSW mo

We further decompose the wave field into a coherent and incoherent component. The coherent part is obtained by applying an expectation operator $\mathbb{E}$ to the complex wave amplitude:

$$\boldsymbol{q}_{coh,\omega}(t) = \Re(\mathbb{E}[\tilde{\boldsymbol{q}}_\omega]e^{i\omega t}), \tag{3}$$

while the incoherent part is the residual:

$$\boldsymbol{q}_{\omega incoh,\omega}(t) = \Re\boldsymbol{q}_\omega(t) - \boldsymbol{q}_{coh,\omega}(t) = \tilde{\boldsymbol{q}}_\omega{}'(t)e^{i\omega t}), \tag{4}$$

where $\tilde{\boldsymbol{q}}_\omega(t)$ is the slowly varying complex wave amplitudevector. These complex wave amplitudes can be extracted $\tilde{\boldsymbol{q}}'_\omega(t) = \tilde{\boldsymbol{q}}_\omega(t) - \mathbb{E}[\tilde{\boldsymbol{q}}_\omega]$ is the incoherent complex amplitude. Ergodicity is assumed throughout the manuscript so that $\mathbb{E}$ is equivalent to a time average $\lim_{T\to\infty}\frac{1}{T}\int_0^T$. Under this assumption, and from the definition (Eq. **??**), we recover the fact that the coherent wave is phase-locked to a monochromatic forcing with frequency ω.

The timescale separation between the mesoscale and the wave allows extracting the complex wave amplitude from the data $\boldsymbol{q} = (u, v, h)^T$ by complex demodulation: a complex demodulation technique:

$$\tilde{\boldsymbol{q}}_\omega = 2\langle \boldsymbol{q}e^{-i\omega t}\rangle, \tag{5}$$

where $< \cdot >$ is a low-pass filter (in time) selecting the potentially broaden broadband spectrum of the wave. This complex wave amplitude can be further decomposed into a coherent component $\mathbb{E}[\tilde{\boldsymbol{q}}_\omega]$, where $\mathbb{E}$ is the expectation operator, and the fluctuations which correspond to the incoherent component of the wave field.

2.3 Non-linear interactions terms

2.3 Equations for the complex wave amplitude

We propose in this section a simple investigation of the non-linear interaction terms leading to the ansatz of From the RSW model (Eq. , highlighting how these terms act to produce the incoherent wave field. To this aim, we perform a linearisation of equations Eq. assuming that waves are of small amplitude. For more generality, a similar development can be performed by only assuming a time scale separation between the two dynamics and a small Froude number $F_r = U_\omega/\sqrt{B_u} \ll 1$ for the wave, where U_ω is the typical amplitude of the wave velocity $\boldsymbol{u}_\omega$ (see **?**).For the present discussion, however, a standard linearisation appears to be sufficient to link the complex demodulation procedure and the role of quadratic non-linearities in the scattering process. We are looking for solutions of the RSW Eqs. of the form **??**), we derive idealised equations for the coherent and incoherent complex amplitudes in order to provide a theoretical framework for the interpretation and justification

of the extended POD method presented in Sect. **??**. Yet, a reader more interested in the estimation algorithm could skip this section and go directly to the description of the extended POD technique (Sect. **??**).

2.3.1 Mesoscale / wave separation

In order to simplify forthcoming developments, we assume that the wave field is of small amplitude. This hypothesis allows to separate the equations into one for the mesoscale flow and one for the waves (possible relaxation of this hypothesis will be discussed below). The state vector is decomposed as $\boldsymbol{q} = \boldsymbol{q}_{jet} + \epsilon \boldsymbol{q}_\omega$, where $\boldsymbol{q}_{jet}$ is the slow ~~jet current component , $\boldsymbol{q}_\omega$ are the perturbative waves,~~ mesoscale component and ϵ is the small parameter of the perturbation expansion. ~~The forcing wave~~ Likewise, the forcing term is also ~~at order ϵ and we consider it time-harmonic of the form $\boldsymbol{q}_{frc,\omega} = \Re(\tilde{\boldsymbol{q}}_{frc,\omega}(x,y)e^{i\omega t})$~~ of order $\mathcal{O}(\epsilon)$.

~~Order 0 approximation leads to~~ At leading order, one obtains the following equation for the ~~slow dynamics~~ mesoscale flow (which is not the focus of the study):

$$\partial_t h_{jet} + B_u \mathrm{div}(\boldsymbol{v}_{jet}) = -R_o \left[(\boldsymbol{v}_{jet}\cdot\nabla) h_{jet} + h_{jet}\ \mathrm{div}(\boldsymbol{v}_{jet}) \right] \tag{6a}$$

$$\partial_t \boldsymbol{v}_{jet} + (1+\beta y)\boldsymbol{v}_{jet}^\perp + \nabla h_{jet} = -R_o (\boldsymbol{v}_{jet}\cdot\nabla)\boldsymbol{v}_{jet}. \tag{6b}$$

~~and a wave equation~~ The equation for the wave is obtained at order ~~1~~ϵ^1:

$$\partial_t h_\omega + B_u \mathrm{div}(\boldsymbol{v}_\omega) = -R_o \left[(\boldsymbol{v}_{jet}\cdot\nabla) h_\omega + (\boldsymbol{v}_\omega\cdot\nabla) h_{jet} + h_{jet}\ \mathrm{div}(\boldsymbol{v}_\omega) + h_\omega\ \mathrm{div}(\boldsymbol{v}_{jet}) \right] + h_{frc,\omega} f_{h,\omega} \tag{7a}$$

$$\partial_t \boldsymbol{v}_\omega + (1+\beta y)\boldsymbol{v}_\omega^\perp + \nabla h_\omega = -R_o \left[(\boldsymbol{v}_{jet}\cdot\nabla)\boldsymbol{v}_\omega + (\boldsymbol{v}_\omega\cdot\nabla)\boldsymbol{v}_{jet} \right] + {}_{frc,\omega}\boldsymbol{f}_{\boldsymbol{v},\omega}. \tag{7b}$$

~~Let us now derive a simple equation for the incoherent complex wave amplitudes.~~ For conciseness, we ~~first write Eq.~~ rewrite the above system of equations in terms of linear and bilinear operators:

$$\partial_t \boldsymbol{q}_\omega + \boldsymbol{L}(\boldsymbol{q}_\omega) = -R_o \boldsymbol{B}(\boldsymbol{q}_{jet}, \boldsymbol{q}_\omega) + {}_{frc,\omega}\boldsymbol{f}_{\boldsymbol{q},\omega}, \tag{8}$$

with,

$$\boldsymbol{L}(\boldsymbol{q}_\omega) = \begin{pmatrix} B_u \mathrm{div}(\boldsymbol{v}_\omega) \\ (1+\beta y)\boldsymbol{v}_\omega^\perp + \nabla h_\omega \end{pmatrix}, \quad \boldsymbol{B}(\boldsymbol{q}_{jet}, \boldsymbol{q}_\omega) = \begin{pmatrix} (\boldsymbol{v}_{jet}\cdot\nabla) h_\omega + (\boldsymbol{v}_\omega\cdot\nabla) h_{jet} + h_{jet}\ \mathrm{div}(\boldsymbol{v}_\omega) + h_\omega\ \mathrm{div}(\boldsymbol{v}_{jet}) \\ (\boldsymbol{v}_{jet}\cdot\nabla)\boldsymbol{v}_\omega + (\boldsymbol{v}_\omega\cdot\nabla)\boldsymbol{v}_{jet} \end{pmatrix}.$$

~~Here,~~ $\boldsymbol{L}$ is a linear operator and $\boldsymbol{B}$ is a symmetric bilinear map associated to the non-linear interactions with the jet. ~~From this equation, we can readily write~~ Finally, we derive an equation for the wave amplitude by injecting the ~~wave ansatz~~ ansatz Eq. (**??**) into Eq. (**??**)~~and multiplying the result by $e^{-i\omega t}$, and low pass filtering, thus obtaining:~~ , then performing a complex demodulation operation Eq. (**??**), with a filter eliminating dynamics at frequencies higher than typical mesoscale frequencies, (*e.g.* frequencies at 2ω resulting from complex demodulation). This repeats the hypothesis (Sect. **??**) that the frequency ω of IT is much higher than the frequencies of mesoscale flows. We thus obtain:

$$\partial_t \tilde{\boldsymbol{q}}_\omega + i\omega\tilde{\boldsymbol{q}}_\omega + \boldsymbol{L}(\tilde{\boldsymbol{q}}_\omega) = -R_o \boldsymbol{B}(\boldsymbol{q}_{jet}, \tilde{\boldsymbol{q}}_\omega) + {}_{frc,\omega}\tilde{\boldsymbol{f}}_{\boldsymbol{q},\omega}. \tag{9}$$

~~Now decomposing~~

2.3.2 Equations for the coherent and incoherent waves

A Reynolds decomposition of the jet component into a mean ~~part $\mathbb{E}[\boldsymbol{q}_{jet}]$, where $\mathbb{E}$ is an expectation operator,~~ and a fluctuating part ~~$\boldsymbol{q}'_{jet} = \boldsymbol{q}_{jet} - \mathbb{E}[\boldsymbol{q}_{jet}]$ gives the following equation:~~

$$\partial_t \tilde{\boldsymbol{q}}_\omega + i\omega\tilde{\boldsymbol{q}}_\omega + \boldsymbol{L}(\tilde{\boldsymbol{q}}_\omega) + R_o\boldsymbol{B}(\mathbb{E}[\boldsymbol{q}_{jet}], \tilde{\boldsymbol{q}}_\omega) = -R_o\boldsymbol{B}(\boldsymbol{q}'_{jet}, \tilde{\boldsymbol{q}}_\omega) + \tilde{\boldsymbol{q}}_{frc,\omega}.$$

~~We now make the assumption that the wave amplitudes evolves on slow time scales compared to the wave period $2\pi/\omega$ (which can be formalized more rigorously by a WKBJ approach). This allows us to write:~~

$$\tilde{\boldsymbol{q}}_\omega = -R_o\boldsymbol{R}\boldsymbol{B}(\boldsymbol{q}'_{jet}, \tilde{\boldsymbol{q}}_\omega) + \boldsymbol{R}\tilde{\boldsymbol{q}}_{frc,\omega},$$

~~where $\boldsymbol{R} = [i\omega I + \boldsymbol{L} + \boldsymbol{B}(\mathbb{E}[\boldsymbol{q}_{jet}], \cdot)]^{-1}$ is the resolvent operator, with $i\omega$ assumed not to be an eigenvalue of $\boldsymbol{L} + \boldsymbol{B}(\mathbb{E}[\boldsymbol{q}_{jet}], \cdot)$. Thus, under the hyptoheses of small wave amplitude (or Froude number) and timescale separation between the wave period and the jet fluctuations, we find that the evolution of the complex amplitudes reflects instantaneously the jet fluctuations through the nonlinear interaction term and the resolvent operator. It can be noted that this time scale separation can also be interpreted by the fact that the resolvent operator is approximately constant over the frequency band considered for the broadband scattered wave .~~

~~Separating the wave solution into a $\boldsymbol{q}_{jet} = \mathbb{E}[\boldsymbol{q}_{jet}] + \boldsymbol{q}'_{jet}$,~~ and of the wave into its coherent and incoherent ~~contribution $\tilde{\boldsymbol{q}}_\omega = \mathbb{E}[\tilde{\boldsymbol{q}}_\omega] + \tilde{\boldsymbol{q}}'_\omega$ and taking the~~ part $\tilde{\boldsymbol{q}}_\omega = \mathbb{E}[\tilde{\boldsymbol{q}}_\omega] + \boldsymbol{q}'_\omega$, gives the following equation:

$$\partial_t \tilde{\boldsymbol{q}}'_\omega + i\omega(\mathbb{E}[\tilde{\boldsymbol{q}}_\omega] + \tilde{\boldsymbol{q}}'_\omega) + \boldsymbol{L}(\mathbb{E}[\tilde{\boldsymbol{q}}_\omega] + \tilde{\boldsymbol{q}}'_\omega) + R_o\boldsymbol{B}(\mathbb{E}[\boldsymbol{q}_{jet}], \mathbb{E}[\tilde{\boldsymbol{q}}_\omega] + \tilde{\boldsymbol{q}}'_\omega) = -R_o\boldsymbol{B}(\boldsymbol{q}'_{jet}, \mathbb{E}[\tilde{\boldsymbol{q}}_\omega] + \tilde{\boldsymbol{q}}'_\omega) + \tilde{\boldsymbol{f}}_{\boldsymbol{q},\omega}. \tag{10}$$

Taking the expectation operator of Eq. (**??**) leads to an equation for the coherent wave amplitude ~~:~~ (where the expectation of the derivative va

$$i\omega\mathbb{E}[\tilde{\boldsymbol{q}}_\omega] + \boldsymbol{L}(\mathbb{E}[\tilde{\boldsymbol{q}}_\omega]) + R_o\boldsymbol{B}(\mathbb{E}[\boldsymbol{q}_{jet}], \mathbb{E}[\tilde{\boldsymbol{q}}_\omega]) = -R_o\mathbb{E}[\boldsymbol{B}(\boldsymbol{q}'_{jet}, \tilde{\boldsymbol{q}}'_\omega)] + \tilde{\boldsymbol{f}}_{\boldsymbol{q},\omega} \tag{11a}$$

$$\mathbb{E}[\tilde{\boldsymbol{q}}_\omega] = \boldsymbol{R}\big[\tilde{\boldsymbol{f}}_{frc,\omega} - R_o\mathbb{E}[\boldsymbol{B}(\boldsymbol{q}'_{jet}, \tilde{\boldsymbol{q}}'_\omega)]\big], \tag{11b}$$

~~This~~ where $\boldsymbol{R} = [i\omega I + \boldsymbol{L} + \boldsymbol{B}(\mathbb{E}[\boldsymbol{q}_{jet}], \cdot)]^{-1}$ is the resolvent operator, which allows us to write the equation in a more compact form. The resolvent operator can be viewed as the integral operator associated with the Green's function (**?**), and is well defined if $-i\omega$ is not an eigenvalue of $\boldsymbol{L} + \boldsymbol{B}(\mathbb{E}[\boldsymbol{q}_{jet}], \cdot)$. This equation means that the coherent wave ~~amplitude~~ field is the sum of the linear response ~~of the forcing $\tilde{\boldsymbol{q}}_{frc,\omega}$, and an averaged non-linear correction involving~~ to the forcing $\tilde{\boldsymbol{f}}_{\boldsymbol{q},\omega}$, and of the averaged interaction be the jet fluctuations and the incoherent ~~part~~wave field.

Finally, ~~substracting this equation~~ subtracting Eq. (**??**) to Eq. (**??**) leads to the equation for the incoherent wave amplitude:

$$\partial_t \tilde{\boldsymbol{q}}'_\omega + i\omega\tilde{\boldsymbol{q}}'_\omega + \boldsymbol{L}(\tilde{\boldsymbol{q}}'_\omega) + R_o\boldsymbol{B}(\mathbb{E}[\boldsymbol{q}_{jet}], \tilde{\boldsymbol{q}}'_\omega) = -R_o\boldsymbol{B}(\boldsymbol{q}'_{jet}, \mathbb{E}[\tilde{\boldsymbol{q}}_\omega]) - R_o\boldsymbol{B}(\boldsymbol{q}'_{jet}, \tilde{\boldsymbol{q}}'_\omega) + R_o\mathbb{E}[\boldsymbol{B}(\boldsymbol{q}'_{jet}, \tilde{\boldsymbol{q}}'_\omega)] \tag{12a}$$

$$\boldsymbol{R}\partial_t \tilde{\boldsymbol{q}}'_\omega(t) + \tilde{\boldsymbol{q}}'_\omega(t) = \underbrace{R_o\boldsymbol{R}\big[\mathbb{E}[\boldsymbol{B}(\boldsymbol{q}'_{jet}(t), \tilde{\boldsymbol{q}}'_\omega(t))] - \boldsymbol{B}(\boldsymbol{q}'_{jet}(t), \tilde{\boldsymbol{q}}'_\omega(t))\big]}_{\text{Multiple scattering}} - \underbrace{R_o\boldsymbol{R}\boldsymbol{B}(\boldsymbol{q}'_{jet}(t), \mathbb{E}[\tilde{\boldsymbol{q}}_\omega])}_{\text{single scattering}}. \tag{12b}$$

In this equation, the non-linear interactions are decomposed into a ~~primary~~ single scattering term, which is the interaction between the coherent wave $\mathbb{E}[\tilde{\boldsymbol{q}}_\omega]$ and the jet fluctuations, and a multiple scattering term which is the interaction with the jet fluctuations and the incoherent wave component. ~~It can be noted that the single scattering term only involves the coherent wave part (in addition to the jet fluctuations): thus, the fluctuations of the wave field (*i.e.* the incoherent wave field) are driven by the fluctuations of the jet. This decomposition of the wave response to the nonlinear interactions with the fluctuating jet will be exploited in Sect. **??**, in order to provide grounds for using the EPOD method to analyse and estimate the coupled wave/jet fluctuations.~~

3 ~~Methods~~

~~This section details the data-driven methods applied to investigate the wave variability due to a scattering by a jet . We should stress that it is important to capture the broadband spectrum~~ If we now neglect the slow variations in the complex amplitude, assuming that they evolve over long time scales relative to the wave period $2\pi/\omega$, we obtain the reduced equation:

$$\tilde{\boldsymbol{q}}'_\omega(t) = \underbrace{R_o\boldsymbol{R}\big[\mathbb{E}[\boldsymbol{B}(\boldsymbol{q}'_{jet}(t),\tilde{\boldsymbol{q}}'_\omega(t))] - \boldsymbol{B}(\boldsymbol{q}'_{jet}(t),\tilde{\boldsymbol{q}}'_\omega(t))\big]}_{\text{Multiple scattering}} - \underbrace{R_o\boldsymbol{R}\boldsymbol{B}(\boldsymbol{q}'_{jet}(t),\mathbb{E}[\tilde{\boldsymbol{q}}_\omega])}_{\text{single scattering}}. \tag{13}$$

It can be noted that this time scale separation can also be interpreted as assuming that the resolvent operator is approximately constant o This approximation consists in considering a jet "frozen" with respect to the propagation time of the wave ~~field in order to study its dynamics and the scattering by the turbulent low-frequency dynamics. Indeed, in time frequency-space, the operator $\boldsymbol{B}$ in Eqs. to is a convolution operator between the dynamics of~~ to travel the domain. It becomes limiting in large domains where the propagation It is the limit of the use of instantaneous correlations between the jet and the wave in the ~~wave and the jet. Under its action, the spectrum of an incident harmonic wave at frequency ω, as we consider in this study, represented by a Dirac in spectral space, is broadened by convolution with the slow dynamics.The nearby frequencies around ω are then associated to the incoherent components. Authors in the oceanographic literature often design the broadband spectrum of IT as "cusps". This has been highlighted in particular in **??** by investigating spectra of high-resolved time records of Sea Level Height, showing that the incoherent frequency were actually not as low as expected. The spectral broadening of a scattered field has also been studied in various fluid mechanics contexts such as in **??**, for non-dispersive waves.~~

~~It is thus necessary to design an algorithm that captures all these effects of triadic interactions with the jet , which is one of the motivation of the BBPOD algorithm, proposed~~ EPOD method Sect. **??** and is referred to as local scattering hypothesis.

The above developments can be justified without assuming a small wave amplitude, but asymptotically from the assumption of separation of time scales, using perturbation theory (chapter 4 of **?**). This involves introducing the change of variable $\tilde{\boldsymbol{q}}_\omega(\epsilon t)$ and retaining the dominant term of a multiscale decomposition of the wave. As a consequence, Reynolds stresses remain at order 0, and gen A similar separation of equations has been generalized to high amplitude waves by multiple-scale analysis in **?** in a 1-layer quasi-geostrophi **??** for RSW models, and in Sect. 2 of **?** for a primitive equations model in view of investigating the impact of internal waves on the balance It can be noticed that this is not a critical issue since we focus on the impact of the jet flow on the wave (and not the inverse),

and because the identified modes are extracted by modal decomposition from the non-linear simulation, as it will be presented in Sect. ?? below, which precisely extracts the optimal modes in a energetic sense for large frequency bands dynamics. The description of the EPOD method follows ?, to extract correlation within the data, adapted here to the case of wave-flow interaction. Finally, a simple algorithm of estimation is presented in ??.

3 Methods

This section details the data-driven methods, derived from POD, that are adapted to decompose a wave scattered by a turbulent flow. These methods are the Broadband POD (BBPOD – Sect. ??, where the modal decompositions that are presented define an observation operator to estimate the two dynamics from a non-filtered observation.??) and the Extended POD (EPOD– Sect. ??). We then propose an algorithm that uses these decompositions to disentangle the mesoscale flow and the wave field from SSH observations (Sect. ??).

3.1 The Broadband POD method

The algorithm that we call Broadband POD (BBPOD) consists of performing a POD on a complex demodulated (wave) field, in order to capture the its most energetic modes of variability of this wave field from numerical from time series data. This algorithm can be viewed as a enables capturing the finite-width frequency-band dynamics with a single basis. The proposed algorithm can be related to the spectral proper orthogonal decomposition (**??**), but which is adapted to optimally represent finite width frequency band dynamics. The connection between the two algorithm is detailed in appendixas detailed in Appendix **??**. This algorithm It is also similar to a POD applied to wavelet transformed data on wavelet-transformed (in time) variables, in the sense that the complex demodulation also providesthe content provides, like the wavelet transform, a temporal description of the signal at a given frequency ω. A wavelet EOF analysis of ocean waves has been performed in particular in ??applied either to Such a method has been applied in the context of ocean internal waves by **??**, who named the method "wavelet EOF" and performed the transformation either along the vertical direction or in time the time coordinate.

We consider a set of data $\boldsymbol{q}$, assumed to be statistically stationary (at least first and second order), and containing a broadband peak centered around a frequency ω. The algorithm of BBPOD to extract the coherent structures evolving to build a BBPOD basis at frequency ω is made of consists of the following steps. We first compute the complex demodulation of $\boldsymbol{q}$ at the frequency ω, $\tilde{\boldsymbol{q}}_\omega$ (Eq. **??**), with the choice of an appropriate filter to capture the broadband structure of the data. We assume that the slowly varying wave amplitude is statistically stationary (at least first and second order), which is a requirement for the POD technique (**?**). We next compute the space auto-correlation tensor of the complex amplitudes:

$$\mathbf{C}(x,y,x',y') = \mathbb{E}[\tilde{\boldsymbol{q}}_\omega(x,y,t) \otimes \tilde{\boldsymbol{q}}^*_\omega(x',y',t)], \tag{14}$$

where $\otimes$ is the dyadic product, product of the components $(q_i q_j)_{i,j}$, and the superscript $\cdot^*$ denotes the transpose-conjugate operation. HereAs mentioned in Sect. **??**, the expectation operator $\mathbb{E}$ is computed as a mean over time under the ergodicity hypothesis in the present paper.

Before solving the POD problem, we define an innerproduct representative of the quadratic energy E of the model Eq. (**??**), encoded with a positive definite matrix $\mathbf{W}_E$:

$$\|\boldsymbol{q}\|^2_{\mathbf{W}_E} = (\boldsymbol{q}, \mathbf{W}_E \boldsymbol{q})_{L^2(\Omega)} = \frac{1}{2}\int_\Omega (u^2+v^2)\,\mathrm{d}x\mathrm{d}y + \frac{1}{2B_u}\int_\Omega h^2\,\mathrm{d}x\mathrm{d}y. \tag{15a}$$

This norm corresponds to the kinetic plus potential energy for a small perturbation (*e.g.* **?**). The BBPOD modes $(\boldsymbol{\psi}_{n,\omega})_n$ are then defined as the solution ~~of~~ to the Fredholm equation:

$$\int_\Omega \mathbf{C}(x,y,x',y')\mathbf{W}_E(x',y')\boldsymbol{\psi}_{n,\omega}(x',y')\,\mathrm{d}x'\mathrm{d}y' = \lambda_{n,\omega}\boldsymbol{\psi}_{n,\omega}(x,y), \tag{16}$$

with non-negative eigenvalues $\lambda_{n,\omega}$. The BBPOD modes form an orthonormal basis of square integrable functions (in space) ~~,~~ respectively to the innerproduct defined in Eq (**??**). The complex demodulated field can be expressed by the decomposition:

$$\tilde{\boldsymbol{q}}_\omega(t,x,y) = \sum_{n=0}^{\infty} a_{n,\omega}(t)\boldsymbol{\psi}_{n,\omega}(x,y), \tag{17}$$

where ~~$a_{n,\omega}(t) = \int_\Omega \boldsymbol{\psi}^*_{n,w}\mathbf{W}_E\tilde{\boldsymbol{q}}_\omega(t)dxdy$~~ is the n-th $a_{n,\omega}(t) = \int_\Omega \boldsymbol{\psi}^*_{n,w}(x,y)\mathbf{W}_E\tilde{\boldsymbol{q}}_\omega(t,x,y)\mathrm{d}x\mathrm{d}y$ is the n-th projection coefficient. The modes are also decorrelated from each other and are optimal to express the quadratic mean energy at frequency ω, calculated as:

$$\mathbb{E}(\|\tilde{\boldsymbol{q}}_\omega\|^2_{\mathbf{W}_E}) = \sum_{n=0}^{\infty}\lambda_{n,\omega}. \tag{18}$$

~~An important simplification arises in the presence of an homogeneous direction, that is if the statistics do not depend on a coordinate. For our idealised test case, where the x direction is homogeneous, the BBPOD modes dependence along this direction reduces to Fourier modes of the form $e^{ik_x x}$, where k_x are wavenumbers. Yet this property is not leveraged in this study, as in Sect.**??** will be presented an algorithm to estimate the low and high frequency dynamics for the most general wave-flow configuration. The reader can refer to the literaturefor more details of the theoretical background of POD methods (**???**).~~

~~Lastly, in the literature,~~ In practice, the method of snapshots (**?**) is considered for numerical implementation. In the literature, POD usually applies to a zero-mean process, and the mean is subtracted beforehand from the data. However, ~~if~~ provided the mean field is solution ~~of~~ to the Fredholm equation above (Eq. **??**), the procedure remains unchanged if we consider the total field or only the fluctuations. ~~For more generality, and because~~ Since the mean quantities are relevant both to examine ~~our problem of~~ the wave scattering and for the ~~estimations~~ estimation algorithm presented in Sect.**??**, **??**, we keep the total field ~~is considered here.~~ in our application. The reader can refer to the literature for more details on the theoretical backgrounds of POD methods (**???**).

3.2 The extended POD method

~~In its original form,~~

In this section, we present the Extended POD method (**?**), which consists of extracting the component of a signal that is correlated with a POD mode of a second signal. Here, we apply this method to the context of wave-current interactions by expressing a decomposition of the wave correlated to a POD decomposition of the mesoscale flow. There is indeed a natural correlation between these two components, as the ~~extended POD (EPOD) method (see **?**) extracts, from a target field representing any physical quantities (*e.g* pressure), the contribution correlated to a given POD basis computed from any other quantity (*e.g* velocity). It is adapted here to the analysis of a wave scattered by a turbulent background flow. Indeed, as stated previously (Eq. **??**), the incoherent contribution~~ variability of the wave field is ~~generated by the jet through the bilinear form~~ driven by the mesoscale fluctuations via the bilinear term $\boldsymbol{B}(\boldsymbol{q}_{jet}, \tilde{\boldsymbol{q}}_\omega)$ ~~. The EPOD method can thus be leveraged to exploit this correlation to estimate the fluctuation of the wave field knowing the fluctuations of the jet, or conversely. Here, we propose to extract the part of the wave correlated to the jet component, by the computation of its EPOD modes, forming a decomposition of the wave correlated to a~~ in Eq. (**??**).

Given a POD decomposition of the ~~jet component. The jet component is extracted from data by a low-pass filter.~~ ~~The~~ mesoscale flow, the n-th ~~EPOD mode~~ extended POD mode of the wave is defined by:

$$\boldsymbol{\chi}_n(\tilde{\boldsymbol{q}}_\omega, \boldsymbol{q}_{jet}) = \frac{\mathbb{E}[\tilde{\boldsymbol{q}}_\omega\, a_n]}{\lambda_n} \frac{\mathbb{E}[\tilde{\boldsymbol{q}}_\omega(t,x,y)\, a_n(t)]}{\lambda_n}, \tag{19}$$

where ~~a_n~~ $a_n(t) \in \mathbb{R}$ is the projection coefficient of the jet component onto its POD basis at time t (for the innerproduct defined in Eq. (**??**)) and λ_n is the associated eigenvalue. ~~As~~ In order to lighten the notation in the following, we will drop the second argument $\boldsymbol{q}_{jet}$ and denote by $\boldsymbol{\chi}_n(\tilde{\boldsymbol{q}}_\omega)$ the n-th EPOD mode. As stated before, the expectation operator is a time average in this study. As the POD modes of the jet are decorrelated ~~between each other~~from one another, the n-th EPOD contribution ~~$a_n\boldsymbol{\chi}_n(\tilde{\boldsymbol{q}}_\omega, \boldsymbol{q}_{jet})$~~ $a_n\boldsymbol{\chi}_n(\tilde{\boldsymbol{q}}_\omega)$ is the part of the wave correlated to the n-th POD mode of the jet, but completely decorrelated ~~to the other~~ from the other POD modes of the jet. It provides a decomposition of the wave component $\tilde{\boldsymbol{q}}_{c,\omega}$ that is correlated with the ~~N-order~~ N-order truncation POD decomposition of the turbulent jet:

$$\tilde{\boldsymbol{q}}_{c,\omega}(t,x,y) = \sum_{n=0}^{N} a_n(t)\boldsymbol{\chi}_n(\tilde{\boldsymbol{q}}_\omega)(x, {}_{jet}y). \tag{20}$$

~~It can be noted that this procedure filter~~This decomposition filters out all wave contributions decorrelated from the jet ~~(incoming~~ on Ω. These may come from outside the domain ~~for instance). In order to lighten the notation in the following, we will drop the second argument $\boldsymbol{q}_{jet}$ and denote by $\boldsymbol{\chi}_n(\tilde{\boldsymbol{q}}_\omega)$ the n-th EPOD mode.~~or from other sources of variability, such as variations in stratification (**?**).

~~It can be shown~~ We will show now that the EPOD modes of the wave ~~field~~ and the POD modes of the jet are ~~dynamically linked with each other~~ not only correlated between each other but also dynamically linked through the resolvent operator. ~~This confers a strong~~ They are the response to the non-linear interactions between the wave and the jet through scattering, thus conferring an easier interpretation of this correlation-based technique~~, since it highlights an underlying connection between these modes through the dynamical model. To this aim, let us consider the~~ . Let us consider Eq. (**??**) for the incoherent ~~wave~~complex amplitude, in a regime where the multiple scattering terms can be neglected~~(~~, *e.g.* if the ~~incoming wave is~~

~~coherent and the~~ interaction zone remains of limited extent ~~).~~ (?). Taking the expectation of this equation multiplied by a POD coefficient of the fluctuations a'_n associated with mode $\boldsymbol{\psi}'_n = (\psi'_u, \psi'_v, \psi'_h)^T$, one obtains the following equation:

$$\frac{\mathbb{E}[a'_n \tilde{\boldsymbol{q}}'_\omega]}{\lambda'_n} = -R_o \boldsymbol{RB}\left(\frac{\mathbb{E}[a'_n \boldsymbol{q}'_{jet}]}{\lambda'_n}, \mathbb{E}(\omega)\mathbb{E}[\tilde{\boldsymbol{q}}_\omega]\right),$$

that is:

$$\boldsymbol{\chi}_n(\boldsymbol{q}'_\omega) = -R_o \boldsymbol{RB}(\boldsymbol{\psi}'_n, \mathbb{E}(\omega\mathbb{E}[\tilde{\boldsymbol{q}}_\omega])). \tag{21}$$

This equation indicates that the ~~wave EPOD modes are instantaneous responses to the interactions~~ EPOD modes of the incoherent complex amplitude are the instantaneous response to the interaction between the coherent wave and the ~~jet modes, under the hypotheses of a flow dominated by single scattering interactions. This~~ POD modes of the jet fluctuations. We point out that the extended POD modes actually extract multiple scattering interactions from data, but the link with the POD modes of the turbulent fluctuations is then no longer direct. This correspondence has been successfully tested numerically in ? on a configuration similar A dynamical link between POD and EPOD has also been exploited in the context of wall-bounded turbulent flows (?) and turbulent jet flows (?).

~~As a final remark, we shall stress that EPOD modes are optimal for an appropriate innerproduct and vector field. Indeed, the vector $(\boldsymbol{\psi}(\boldsymbol{q}_{jet}), \boldsymbol{\chi}(\tilde{\boldsymbol{q}}_\omega))^T$ is an approximate solution of the POD problem associated to the "extended" vector $(\boldsymbol{q}_{jet}, \tilde{\boldsymbol{q}}_\omega)^T$, with the associated weight matrix $\mathbf{W} = (\mathbf{W}_E, \epsilon\mathbf{W}_E)$, when ϵ goes to 0. For this procedure, POD maximises the energy of the jet contribution, while the wavecomponents are only correlated to the jet field~~ Finally, we would like to point out that numerical calculation of jet POD modes and EPOD modes can be carried out in a single operation. This is done by calculating a POD using the snapshot method on the "extended" vector $(\underbrace{\boldsymbol{q}_{jet}}_{\boldsymbol{W_E}}, \underbrace{\tilde{\boldsymbol{q}}_\omega}_{0})$, without putting any weight on the wave. ~~In the assumption of small wave amplitude, the total energy is essentially the one~~

3.3 Estimation algorithm

We now propose a data-driven method that uses the EPOD formalism to estimate and distinguish the mesoscale and internal tide field from a snapshot of SSH observation. We consider potentially sparse observations: $\mathcal{Y}(t) = h_{obs}(t) = 1_{\Omega_{obs}} h(t)$, where Ω_{obs} is the observation mask.

The proposed method, described in Algorithm **??**, consists of two distinct stages, a training phase (1) and the estimation *per se* (2). In the former, the POD modes of the jet ~~, and we could compute almost identically a POD with weight $\mathbf{W} = (\mathbf{W}_E, \mathbf{W}_E)$, such that $(\boldsymbol{\psi}(\boldsymbol{q}_{jet}), \boldsymbol{\chi}(\tilde{\boldsymbol{q}}_\omega))^T$ are the optimal~~ $\boldsymbol{\psi}(\boldsymbol{q}_{jet})$ and the extended POD modes of the ~~full dynamics. The small wave amplitude is precisely the hypothesis performed in Sect. **??**. This remark motivates using such a basis to perform a full reconstruction of the two motions for a dominant jet, as we propose in the next section.~~ wave field $\boldsymbol{\chi}_n(\tilde{\boldsymbol{q}}_\omega)$ are computed over an initial – "learning" – time window. As in the previous sections (Sect. **??** and **??**), the training dataset is time resolved such that separation The estimation consists in extracting the projection coefficients of the mesoscale part, which link mesoscale modes and IT EPOD modes from observations issued from test set snapshots. We shall stress that the test snapshots do not belong to the training window, but are taken

One may notice that the minimisation method is a simple least-squared regression (**??**), and no regularisation terms are considered . We rely indeed on the "rigid" structure of the problem conferred by the low rank modal decomposition, and the small ratio between number of parameters and size of the observation space.

3.4 ~~Estimation algorithm~~

~~We now present a simple method to estimate IGW and BM from SSH observation in which both signals are entangled, in configurations where this observation is a single snapshot in time with partial coverage in space.~~

~~The observation $\mathcal{Y}$ writes as $\mathcal{Y}(t) = h_{obs}(t) = 1_{\Omega_{obs}} h(t)$, where Ω_{obs} is the mask applied to the observations. The algorithm is as follows:~~

~~As mentioned previously, through the EPOD method, the estimated wave is assumed to be completely correlated to the jet via this algorithm. We take advantage of the presumed strong correlation between the slow BM and the complex incoherent wave amplitude to estimate these two motions, and thereby could enable estimating the IGW field in configurations where the corresponding signal is dominated by a strong background flow. As suggested in **?**, this configuration is challenging for the estimation of the wavefrom real altimetric observations, which is the case for instance~~ A first advantage of this method is that the EPOD decomposition allows the wave to be estimated in configurations where the jet dominates in amplitude. These configurations can be hard for estimating the wave field due to the low signal-to-noise ratio, and also because a strong jet can lead to a very incoherent wave, like in the Gulf Stream region ~~. However, the part of the wave that is completely decorrelated from the jet is not estimated in this algorithm, as it is a quantity that is more difficult to quantify. In addition, velocity fields for both motions can be estimated from SSH by correlation, which thus provides an alternative method to using the geostrophic balance for BM and polarisation relations for IGW. The present algorithm is also minimal and does not require any temporal sampling of the observations. Only a single snapshot is considered to estimate the IGW fields and BM. We also did not made any assumption on the recovering of the coherent wave, which is still a difficult task in regions with strong mesoscale flows (**?**). Yet, if assuming that the coherent wave can be well estimated from observations, it could be substracted from the dataset in the training stage as well as from the observations (estimation stage).~~ (**?**). A second advantage is that the estimation relies on single snapshots, with no assumption about time sampling and/or correlation. Finally, this method also reconstructs – by correlation – the velocity components, from observations of SSH only.

~~Besides, it can be noticed that no regularisation is considered in . We rely indeed on a "rigid" structure of the problem conferred by the modal decomposition, and then a small ratio between number of parameters and size of the observation space. This point will be discussed in the results Sect.**??**, and regularisation term could be added without loss of generality.~~

~~IGW and BM estimates will be shown for an idealised simulation in Sect.**??**, but representative of the configuration of very small amplitude waves. To our knowledge, few studies have addressed the problem of the extraction of an inertia-gravity wave propagating through a strong background flow.~~

4 Numerical results

Algorithm 1 Coupled estimation of IT and mesoscale fields

1. ~~Build the observation operator, representing the superimposition~~ **Training stage**: Compute the POD modes of the jet and the ~~wave component:~~ EPOD modes of the wave field over an initial time window, and construct the observation operator as the superposition of the wave and jet components.

   (a) ~~Perform a POD for the balanced dynamic, noted $\boldsymbol{\psi}_n(\boldsymbol{q}_{jet}) = (\psi_n(\boldsymbol{q}_{jet})_u, \psi_n(\boldsymbol{q}_{jet})_v, \psi_n(\boldsymbol{q}_{jet})_h)^T$~~ Compute the jet POD modes $\boldsymbol{\psi}_n(\boldsymbol{q}_{jet})$

   (b) ~~Compute the complex demodulation of the SSH of the wave , and the associated EPOD mode noted implicitly $\chi_n(\tilde{h}_\omega) = \chi_n(\tilde{h}_\omega, \boldsymbol{q}_{jet})$.~~ Compute the wave EPOD modes: $\boldsymbol{\chi}_n(\tilde{\boldsymbol{q}}_\omega) = (\boldsymbol{\chi}_n(\tilde{\boldsymbol{q}}_\omega)_v, \chi_n(\tilde{\boldsymbol{q}}_\omega)_h)^T$ (consisting of the velocity component and SSH).

   (c) ~~Build the observation operator associated with the N-mode truncation of the SSH field:~~

   ~~Snapshots are approximated as a sum of the contribution of the jet and the wave component for the building of the observation operator. The jet~~ Construct the observation operator $\mathbb{H}$ using N POD/EPOD modes:

   $$\mathbb{H}(\boldsymbol{q}(t)) = \left(\hat{h}_{jet} + \hat{h}_\omega\right) 1_{\{(x,y)\in\Omega_{obs}\}} \tag{22a}$$

   $$= \Re\Big[\sum_{n=0}^{N} a_n(t)\big(\psi_n(\boldsymbol{q}_{jet})_h + \chi_n(\tilde{h}_\omega)e^{i\omega t}\big)\Big] 1_{\{(x,y)\in\Omega_{obs}\}}, \tag{22b}$$

   Here, the jet component is approximated by its ~~POD decomposition truncated at mode N:~~

   ~~$\hat{h}_{jet} = \sum_{n=1}^{N} a_n(t)\psi_n(\boldsymbol{q}_{jet})_h,$~~

   truncated POD decomposition:

   $$\hat{h}_{jet} = \sum_{n=1}^{N} a_n(t)\psi_n(\boldsymbol{q}_{jet})_h,$$

   ~~while the~~ where the hat symbol $\hat{\cdot}$ denotes reconstructed fields. The wave is expressed by ~~its correlation to the jet (following~~ the truncated EPOD decomposition of its complex amplitude (see Eq. ~~)and by adding the coherent fast wave component:~~

   ~~$\hat{h}_\omega = \Re\big[\tilde{h}_{c,\omega}e^{i\omega t}\big]$~~

   ~~$= \Re\big[\sum_{n=0}^{N} a_n(t)\chi_n(\tilde{h}_\omega)e^{i\omega t}\big],$~~

   ??):

   $$\hat{h}_\omega = \Re\big[\tilde{h}_{c,\omega}e^{i\omega t}\big] = \Re\Big[\sum_{n=0}^{N} a_n(t)\chi_n(\tilde{h}_\omega)e^{i\omega t}\Big].$$

   ~~with same a_n as for $\hat{h}_{jet}$.~~

   ~~The observation operator $\mathbb{H}$ then writes as:~~

   ~~$\mathbb{H}(\boldsymbol{q}(t)) = \left(\hat{h}_{jet} + \hat{h}_\omega\right) 1_{\{(x,y)\in\Omega_{obs}\}}$~~

   ~~$= \Re\big[\sum_{n=0}^{N} a_n(t)\big(\psi_n(\boldsymbol{q}_{jeth}) + \chi_n(\tilde{h}_\omega)e^{i\omega t}\big)\big] 1_{\{(x,y)\in\Omega_{obs}\}}.$~~

2. ~~A least-square problem in space is then solved at each time , to find the optimal coefficients that minimise the error with the~~

~~In this section, we present some results on the ability of the previously introduced methods to extract and estimate the IGW and balanced flow field in numerical simulations of the RSW Eqs. .~~ The first part of the results (Sect. **??**) concerns the study of the ~~variability of the IGW field in relation to the turbulent jet fluctuations.~~ BBPOD and EPOD modes from five idealised numerical simulations. We next focus on the estimates of the ~~IGW~~ IT and BM fields (Sect. **??**).

4.1 Numerical configuration

Five numerical simulations of ~~Eqs.~~ the RSW equations (**??**), featuring a plane wave interacting with a zonal jet, have been performed. The parameters that vary from one simulation to another are the temporal frequency of the incoming wave, its direction of propagation, and the Rossby number of the turbulent jet – see Table **??**. The simulations are labelled W1, which is the reference simulation, then W2 to W5. The Burger number is $B_u = 1$ for all simulations (units for space coordinates is therefore the Rossby radius of deformation) ~~.~~ and $\beta = 0.05$. The wave amplitude is small such that wave-wave interactions are negligible. For W1-W4, the jet has approximately the same spectrum and the same energy level, and only the impact of different wave parameters is studied for these runs.

The equations have been discretised using a spectral method in space and a Runge-Kutta time scheme, ~~using~~ with the open-source code Dedalus (**?**). The domain Ω is a doubly periodic rectangular domain of size $[0, 20]\times[-20, 20]$, discretised on a 128×256 grid for W1-W4, and on a 256×1024 grid for W5, which requires a higher resolution. All simulations are initialized with an eastward zonal jet at geostrophic equilibrium with a small perturbation superimposed to trigger its destabilisation. ~~During the experiment, an~~ An eastward wind forcing ~~of the form of~~ term, which is constant in time and follows a Gaussian function in y~~is applied to maintain the balanced current in a stationary state. In order to obtain stationarity, since energy is constantly added by the wind, ~~, and~~ a radiative damping term ~~is added on the continuity equation~~ of the form αh ~~, where α is a constant parameter (following *e.g.* **?**) .~~ (where $\alpha = 10^{-3}$) are added to the system in order to maintain the balanced current in a statistically stationary state (*e.g.* **?**). To ensure numerical stability, a small hyperviscosity diffusion term $-R_o/R_e \frac{1}{1+R_o h}\nabla^4$ is also added in the ~~equations~~momentum equations, with $R_e = 2\cdot 10^5$, following (**?**). The different fields are damped in "sponge layers" at both edges of the y-domain. In particular, βy is linear in the physical domain, and periodicity is ensured in the sponge region through a smooth

The model is first run without wave forcing. Once stationarity is reached (after $4000 f_0^{-1}$, which corresponds approximately to 450 days at mid-latitude), ~~for each simulation a northward propagating plane wave is generated in a nudging layer in the south~~ we activate generation of a plane wave in the sponge layers at the bottom of the domain, which propagates along y before interacting with the jet. The properties of the ~~nudging follows the dispersion relation and the polarisation relation~~ wave forcing follow the dispersion and polarisation relations computed from the harmonic solutions of Eqs. (**??**) linearised around a state at rest. ~~The simulation continues, with snapshots stored every $1/10$ wave period, until the dataset $\boldsymbol{q} = (u, v, h)^T$ contains a sufficiently large number of realisations of the dynamics (corresponding to~~ This second phase of simulation is $4000 f_0^{-1}$ ~~for~~ long for W1-W4 ~~and approximately to~~ and $8000 f_0^{-1}$ for ~~W5). Indeed, like any statistical methods, and in particular for POD methods, the ensemble of realisations has to be sufficiently large so that the BBPOD or EPOD modes computed numerically are well converged. We refer the reader to **?** on convergence issues. Note also that a sufficient sampling in time is required~~

Numerical simulations					
Parameters	W1	W2	W3	W4	W5
Frequency ω	$2f_0$	$3f_0$	$2f_0$	$2f_0$	$2f_0$
Mode number m_x	0	0	1	-1	0
Rossby number R_o	0.2	0.2	0.2	0.2	0.35

Table 1. Parameters of the different simulations.

~~for extracting the complex wave amplitudes by time-filtering in Eq. .~~ W5. Snapshots are saved every 1/10 th of a wave period, enabling extraction of the wave field. The mesoscale part is then extracted (offline) using a low-pass filter (fourth-order Butterworth) with cutoff frequency of $2\pi/10 f_0^{-1}$ (corresponding approximately a period of 3 days at mid-latitude), and the wave field is extracted by complex demodulation at frequency ω (and using the same low-pass filter).

~~The wave is extracted from the outputs of the simulation by complex demodulation around frequency ω, and the jet by a low-pass filter. A fourth-order Butterworth filter is used, discarding frequency above $f_0/10$, corresponding approximately to periods less than 3 days. In Fig.?? is plotted the magnitude~~ Figure ?? shows the power spectrum of the SSH field~~showing the broadband spectral peak associated to the jet~~ , computed using the Welch method with a Hann window of size 160 f_0^{-1} (512 snapshots) with 50% of overlap. It clearly exhibits 2 broadband spectral peaks: one, around $\omega = 0$, associated with the jet and another, around ~~$\omega = 0$ and the wave around~~ $\omega = 2$, ~~highlighting the time scale separation. We notice also the weak super-harmonic signal of IGW (at $\omega = 4$), which we do not address in this study. These simulations are representative of configurations where the wave has weak amplitude compared to the low-frequency dynamics, as described in~~ associated with the wave, and highlights the timescale separation between both flow components that we discussed in Sect. ~~??. For the W1 run for instance,~~ ??. We point out that sub-mesoscale contributions are also extracted by complex demodulation, but these remain negligible. One may also notice that the SSH contribution of the wave ~~represents~~ is only $1-2\%$ of ~~the one of the background flow. For the estimations that are presented in Sect.??, even though the simulations are highly idealised, this is a challenging case to estimate the wave from one entangled observation, due to its very small signal to noise ratio in the observation. This scale separation in amplitude is for example typical of the values that are found in the Gulf Stream region (*c.f.* ?).~~ that of the low-frequency turbulent flow, as well as the presence of a weak super-harmonic signal (at $\omega = 4f_0$), which we do not treat in this study.

~~An example of snapshot associated with the~~ A snapshot of the vorticity field and the complex amplitude of the SSH of the northward prop
reference simulation is ~~shown~~ displayed in Fig.~~??.~~ ??. It shows that the incident wave in the south of the domain is almost plane, while mo

~~In the following,~~

4.2 BBPOD and EPOD analysis

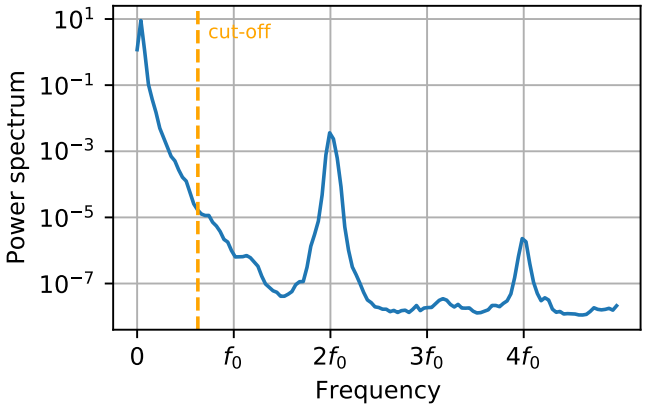

Figure 1. ~~Magnitude~~ Power spectrum of the SSH field in lin-log scale, in the center of the domain $x = 10, y = 0$, for W1. The orange dotted line indicates the filter cut-off frequency.

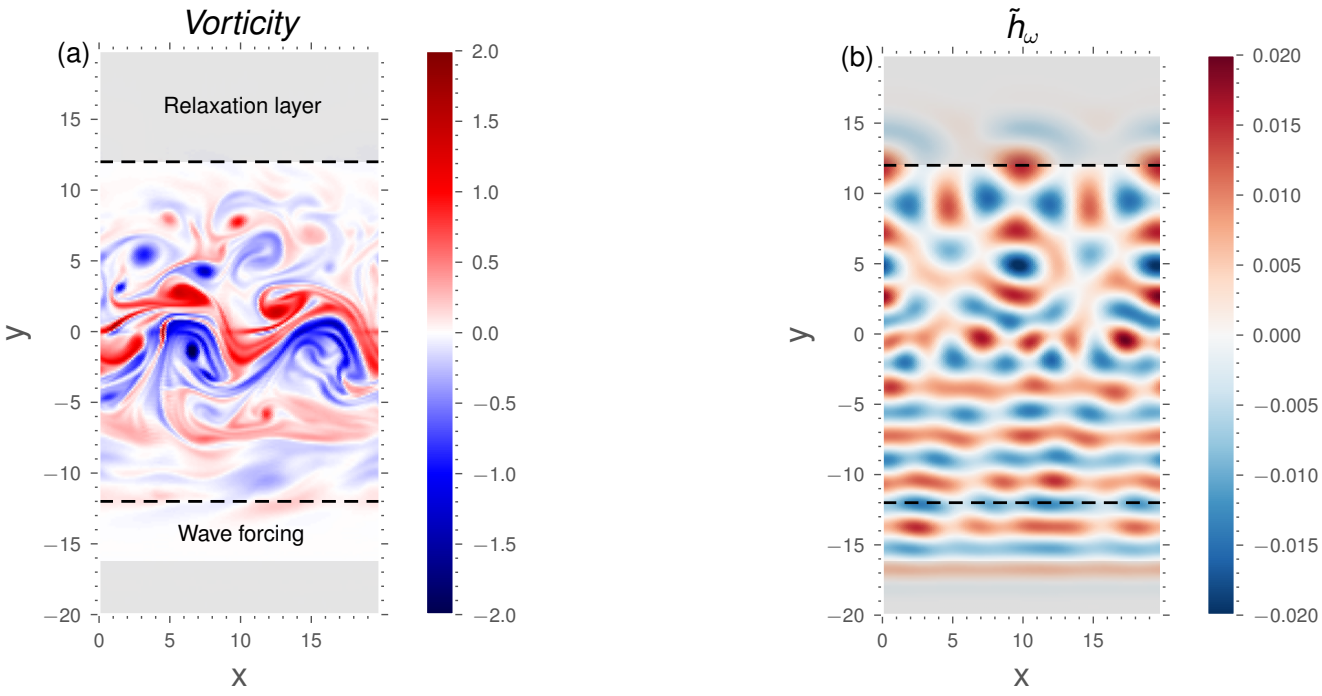

Figure 2. Snapshots of the reference simulation W1 with $\omega = 2f_0, m_x = 0$. ~~In~~ : (**a**) ~~is the~~ total vorticity field and (**b**) ~~shows~~ complex amplitude of the wave SSH contribution. The sponge layer is included in this visualisation for $|y| > 12$, with the wave forcing region in the south and the relaxation

In this section, we show and discuss how the BBPOD and EPOD methods perform in extracting the variability of the wave field, and provide some information on the underlying mechanisms. The modes are computed in the ~~BBPOD modes for the wave will be denoted $(\lambda_{n,\omega}, \psi_{n,\omega})$, while the POD modes of the jet are implicitly denoted (λ_n, ψ_n). They are computed on the~~ physical domain, ~~after removing~~ discarding the sponge regions (for $|y| > 12$).

4.3 ~~BBPOD and EPOD analysis of wave incoherence~~

~~In this section, we study the variability of the wave by means of the computation of its BBPOD and EPOD modes. We analyse the spatio-temporal features extracted from the different simulations, and we make a connection between the low and the high frequency dynamics to understand how the incoherent wave is generated by interaction with a turbulent jet in this context.~~

4.2.1 BBPOD analysis of the wave field

~~In Fig. ?? are presented~~ Figure ?? shows the SSH component of the first three weighted BBPOD modes ($\sqrt{\lambda_{n,\omega}}\psi_{n,\omega}$) of the wave field ~~propagating through the jet, for the different simulations described previously. The leading BBPOD mode , shown on~~ for every simulation. The first dominant mode (the most energetic), in the first column, ~~is the most energetic one in the sense defined in Eq. . In Fig. ?? is plotted the time evolution of the associated leading BBPOD coefficients for W1, and the associated mean and root-mean square values. It shows that the first coefficient is nearly constant and equals its mean values, which indicates that this first mode is phase-locked with the nudging and thereby~~ corresponds to harmonic waves propagating in the same direction as the incident wave. It corresponds to the coherent part of the wave~~field, as commonly defined in the literature and discussed in the previous section ??. As we included in the computation of the energy the incident south part of the wave~~, as confirmed by the time series of the corresponding projection, which is ~~essentially coherent, the whole coherent wave dominates energetically and stands out as the leading BBPOD mode~~ nearly constant in time (see Fig. ??b). We should mention that the fact that the coherent wave is captured by the first BBPOD mode is not guaranteed a priori. Here, it occurs because the energy is integrated over the whole domain, including the lower half of the domain where wave propagation is essentially coherent. ~~Consequently, higher modes are associated with the incoherent part of the wave field and have almost zero mean, as also indicated on Fig. ??. As visible in Fig. ?? (left column), the coherent mode exhibits monochromatic waves (in the x-direction) with the same propagation direction as the incident wave .~~ We can ~~distinguish a drop in amplitude in the north part of the domain, which is particularly pronounced for W3 (with $\omega = 3f_0$)~~ also note a slight damping of the amplitude of the coherent mode for the W2 and W5 ~~. This observation suggests stronger non-linearities, leading to a greater loss of energy to the incoherent waves in this region, which corroborates the analytical results of ? for small scale waves and strong background flows.From left to right the three dominant weighted BBPOD mode of SSH, calculated as $\sqrt{\lambda_{n,\omega}}\psi_{n,\omega}$. From first to last row are the waves W1 to W5.~~ simulations, where the wave is subject to greater interactions. This damping can be interpreted as resulting from the wave-mesoscale correction (last right hand side term in eq. ??).

~~On the second and third column of Fig.?? are shown the two most energetic incoherent modes of each simulation. They are by definition uncorrelated to the first coherent mode. These modes are essentially non-zero in the north domain, and corresponds to nearly-plane waves that are deflected compared to the incident propagation direction with mode number~~

~~$(-2,2),(-2,2),(3,-1),(-3,1)$~~ The sub-optimal modes represent contributions from the incoherent wave, *i.e.* they are a residue of the coherent part which is decorrelated from the wave forcing. The first two dominant incoherent modes exhibit nearly-plane waves deflected by the jet in the upper part of the domain in several directions (where we can also note weak reflections by the jet in the lower half of the domain).

These x-wise structure of these waves is very close to Fourier modes associated with a pair of wavenumbers $m_x = k_x L_x/2\pi$ that are, from top to bottom ~~. Their structure will be investigated later in Fig. **??**, by studying the correlation with the jet. Note that they do not represent perfect~~ $(-2,2),(-2,2),(3,-1),(-3,1)$. This is a consequence of the statistical homogeneity of our configuration (periodic domain, zonal jet), *i.e.* the statistics do not depend on x. This statistical property ensures that the BBPOD modes converge to Fourier modes in ~~the x direction, and slights deviations to a single-mode structure may be due to statistical convergence effects.~~ as the number of snapshots of the correlation matrix increases (**?**).

~~Finally, we complete the description of the BBPOD modes by showing the modal energy distribution of the incoherent wave field, in Fig. **??**, truncated up to 30 modes. The incoherent energy is approximately the same for waves propagating through the flow associated to $R_o = 0.2$, and as expected for the stronger jet the energy is significantly higher. Yet, each mode has a similar contribution on the total energy for each simulation, and the first 10 modes capture a large fraction of it, about $75-85\%$~~

Calculating the eigenvalues of the correlation matrix gives the average energy contribution of each mode (Eq. **??**). We show (Fig. **??**c) the cumulative energy of the incoherent part as a function of the number of modes. This corresponds to the energy contained in the first N incoherent~~part. The slightly less efficiency of the reconstruction for the fast wave $\omega = 3f_0$, and the strong jet , still indicates a more homogeneous modal distribution, consistent with a stronger impact of non-linearities.The graph in Fig. **??** is equivalent to computing the mean-squared error (MSE) at mode N : $MSE = 1 - \sum_{n=1}^{N} \lambda_n / \sum_{n=1}^{+\infty} \lambda_n$.~~ /sub-optimal modes, which is equal to $\sum_{n=1}^{N} \lambda_{n,w}$, whereas λ_0 refers to the energy of the coherent mode. The figure shows first of all that the W5 simulation represents a more energetic incoherent wave than in the other simulations. This can be explained by the fact that the Rossby number is higher and therefore the contribution of the non-linear terms between the wave and the jet responsible for the loss of coherence is a priori also higher (Eq. **??**). Secondly, the figure shows that the incoherent waves from the W1-W4 simulations have a comparable energy level, as the jet is approximately the same.

4.2.2 EPOD analysis

Figure **??** shows the ~~leading three POD modes of the jet,~~ first three dominant jet POD modes and the associated ~~EPOD modes of the complex wave amplitudes for the W1-4 runs. The most energetic~~ wave EPOD modes for simulations W1 to W4. Akin to the dominant wave BBPOD mode shown previously, the first POD mode of the jet is approximately the mean field ~~, and the two suboptimals shown are the dominant meandering structures of the jet, in phase-quadrature with each others. As for the wave, we show in~~ and has nearly constant projection coefficients (Fig. **??** ~~the three first POD coefficients. The leading coefficient is nearly constant in time, and is indeed associated to the mean flow, while the fluctuations are nearly zero mean. Three leading POD modes of the jet (**a**) and the associated EPOD modes of the wave field (**b**) for simulations W1-W4. They are weighted by the square-root of the respective POD eigenvalue of the jet $\sqrt{\lambda_n}$.~~

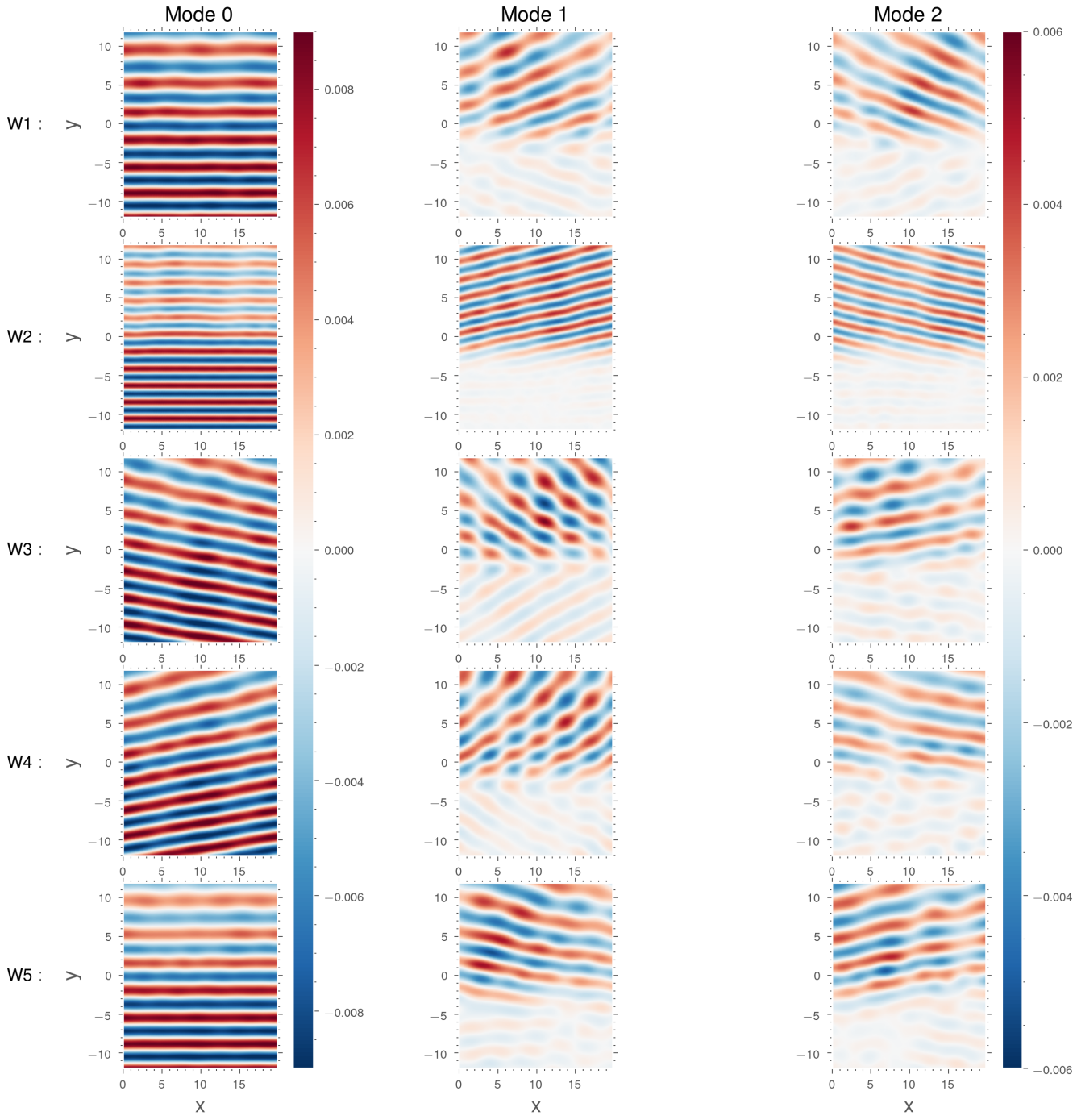

Figure 3. The three dominant weighted BBPOD mode of SSH (left to right), calculated as $\sqrt{\lambda_{n,\omega}}\psi_{n,\omega}$ for the runs W1 to W5 (top to bottom).

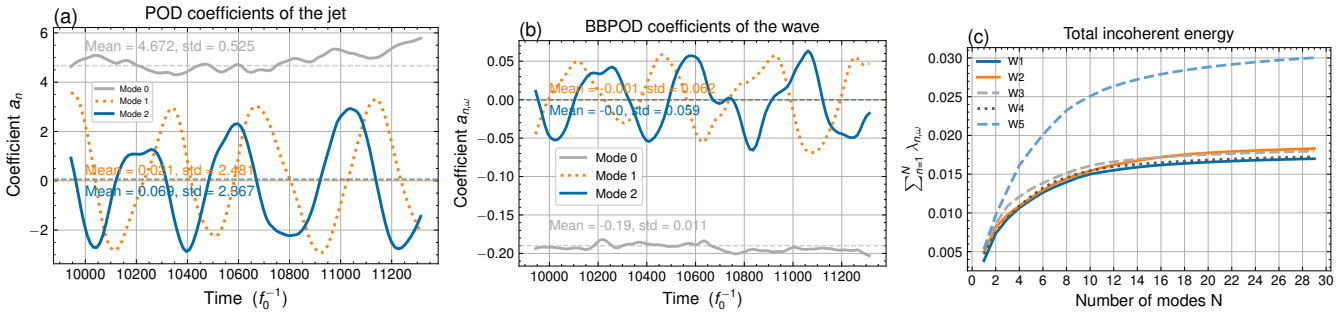

~~Modal energy distribution of the different incoherent wave fields.~~ In (**ac**) ~~is the~~ modal cumulative incoherent energy ~~at mode N:~~ $\sum_{n=1}^{N} \lambda_{n,\omega}$ ~~, and in (**b**) it is normalized by~~ of the ~~total energy:~~ $\sum_{n=1}^{N} \lambda_{n,\omega} / \sum_{n=1}^{+\infty} \lambda_{n,\omega}$ different runs.

~~Modal energy distribution of the different incoherent wave fields.~~ In (**ac**) ~~is the~~ modal cumulative incoherent energy ~~at mode N:~~ $\sum_{n=1}^{N} \lambda_{n,\omega}$ ~~, and in (**b**) it is normalized by~~ of the ~~total energy:~~ $\sum_{n=1}^{N} \lambda_{n,\omega} / \sum_{n=1}^{+\infty} \lambda_{n,\omega}$ different runs.

Figure 4. In (**a**) the three leading BBPOD coefficient of the wave $a_{n,\omega} = (\tilde{\boldsymbol{q}}_\omega, \boldsymbol{\psi}_{n,\omega})_{\mathbf{W}_E}$. In (**b**) the three leading POD coefficient of the jet: $a_n = (\boldsymbol{q}_{jet}, \boldsymbol{\psi}_n)$. They are computed from the reference run W1, and the respective mean values and root-mean squared errors are shown.

~~Modal energy distribution of the different incoherent wave fields.~~ In (**ac**) ~~is the~~ modal cumulative incoherent energy ~~at mode N:~~ $\sum_{n=1}^{N} \lambda_{n,\omega}$ ~~, and in (**b**) it is normalized by~~ of the ~~total energy:~~ $\sum_{n=1}^{N} \lambda_{n,\omega} / \sum_{n=1}^{+\infty} \lambda_{n,\omega}$ different runs.

~~Three leading POD modes of the jet (**a**) and the associated EPOD modes of the wave field (**b**) for simulation W5. They are weighted by the square-root of the respective POD eigenvalue~~ $\sqrt{\lambda_n}$.

~~The lower panel (~~**??b**~~) in Fig. ?? shows that the part~~). The two sub-optimal modes are meanders in phase quadrature. The first EPOD mode of the wave~~correlated to the mean jet is the coherent wave, *i.e.* it is~~ , which is correlated with the mean field, corresponds to the coherent part and has a spatial structure very similar to the ~~leading BBPOD mode of the wave field (left column in Fig. **??**). This readily follows from the fact that both the first jet POD mode wave BBPOD modeessentially capture the mean flow. More interestingly, the~~ first BBPOD mode. The second and third EPOD modes ~~, which are correlated to the meanders , exhibit stationary wave patterns~~ represent the part correlated with the meanders of the jet and feature standing wave patterns along x, which are also in phase quadrature ~~. It is especially remarkable for simulations with an incoming wave perpendicular to the jet~~ suggesting a slow zonal propagation velocity following the jet. This is pronounced in simulations where the wave crosses the jet perpendicularly (W1~~and~~ , W2) ~~, where four nodes are visible along the x direction. Similar patterns are found for~~ with 4 nodes in the domain. For the W5 ~~run in Fig. **??**. However, the meanders have here a twice larger zonal wavelength and also have a weaker energetic contribution (see colorbars). The associated EPOD mode of the wave is a stationary wave with now 2 nodes in the domain. There is thus a clear~~ high Rossby number simulation (shown in Appendix **??**), the jet's sub-optimal modes also represent meanders, and the wave EPOD modes standing wave patterns, both with doubled wavelengths compared to runs W1-W4.

The correspondence between the ~~wavelength of the modes of the jet and the wavelength of the stationary wave. We easily infer from Eq. , that these wave patterns result from the single interaction between each POD mode of the jet and the coherent~~

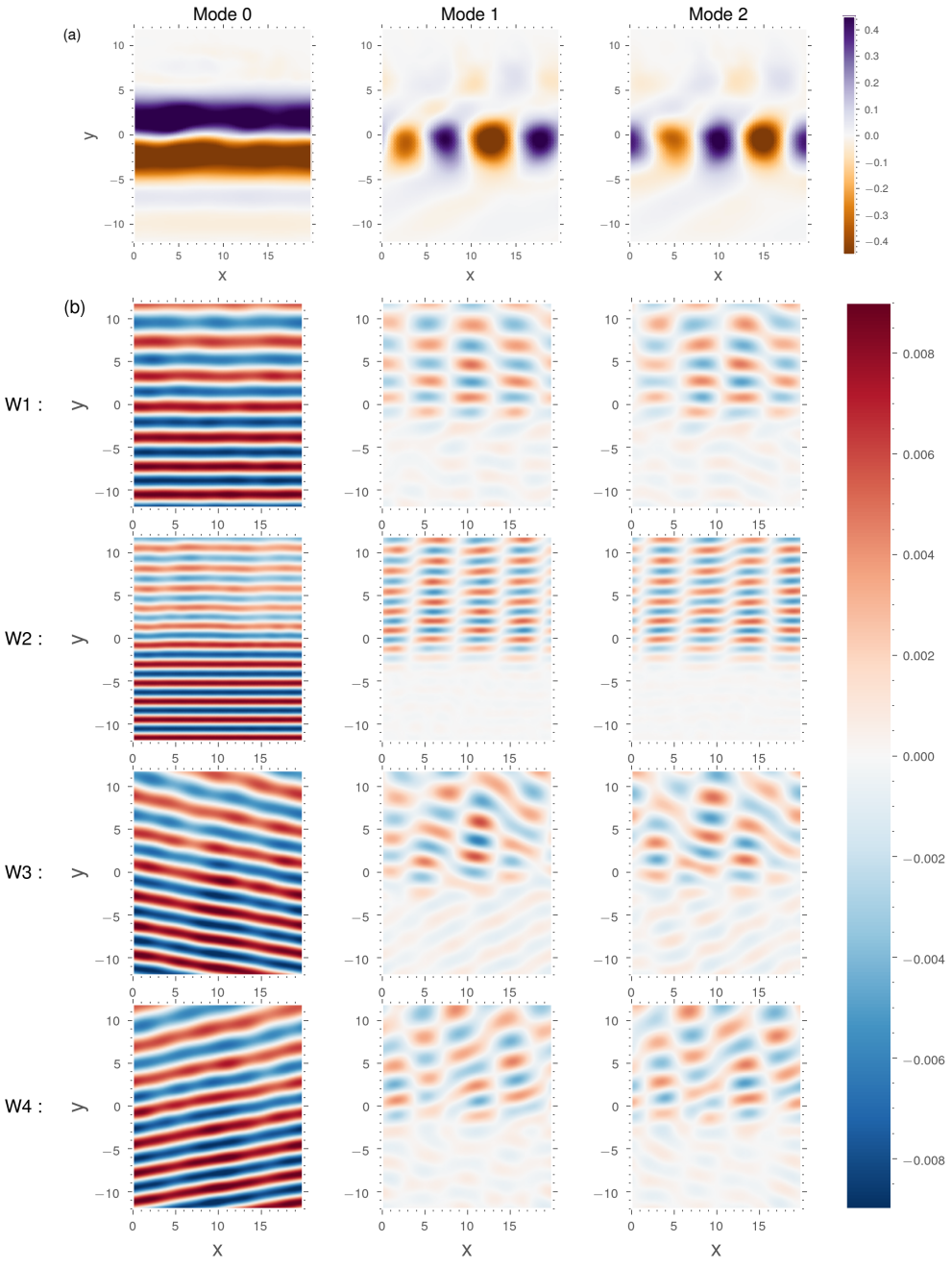

Figure 5. Three leading POD modes of the jet (**a**) and the associated EPOD modes of the wave field (**b**) for simulations W1-W4. They are weighted by the square-root of the respective POD eigenvalue of the jet $\sqrt{\lambda_n}$. The first three eigenvalues are $\lambda_0 = 22.13, \lambda_1 = 6.09, \lambda_2 = 5.59$ for W1 and $\lambda_0 = 22.65, \lambda_1 = 6.77, \lambda_2 = 6.55$ for W2.

wave. As stated theoretically before wavelengths of the jet meanders and those of the EPOD modes confirms the analytical link between these structures that we discussed in Sect. **??** , the EPOD modes computed from these numerical simulations are thus the instantaneous response of the (see Eq. **??**). The dominant wave EPOD modes appear to be the response to interactions between the jet and the coherent wave. All these configurations exhibit a dominance of coherent part and the jet POD modes. The validity of this equivalence suggests that the multiple interaction term is weak for all simulations, which reflects that the mesoscale fluctuations are confined y-wise, such that the scattered wave rapidly leaves this zone, leaving no room for further interaction with the fluctuating jet.

The temporal evolution of the BBPOD wave modes seems to be related to the EPOD/POD behaviour – see Fig. **??**: mode 1 are approximately in phase and mode 2 approximately in phase opposition. Indeed, the standing waves of EPOD modes correspond to the single scattering interactions by comparison with the multiple scattering terms. This probably owes to the fact that the dominant fluctuations patterns are localised in the center of the domain, and therefore the wave that is scattered upward cannot reinteract with these structures. We also infer that the present stationary waves result from the superposition of the two upward upward and downward deflections extracted by the BBPOD method. In detail, in the BBPOD , the two deflections are decorrelated because More precisely, BBPOD extracts these two deviations separately, since they are decorrelated and associated with opposite zonal wavenumbers, which explains this separation in two distinct modes, while they are recovered at once by correlation to the jetmodes. Finally, by looking at the temporal coefficients of the two dynamics in Fig. **??**, sign wave numbers, whereas the EPOD method extracts the superposition of these deviations in a single mode by correlation with the jet. It can be noticed in figure **??**b, that there is a slight phase shift from an exact phase opposition, which corresponds to the slow zonal propagation of the standing wave. By summing these two first modes, we can conclude that the time evolution of the contribution of these meandering modes to the incoherent wave modes seems to be completely driven by the time evolution of the jet modes, the two sharing the same time scale. Therefore, we can state that in these configurations the dominant structures of the jet completely drive the optimal modes of the wave, according to the aforementionned single triad interaction.

Note also the presence of a weak reflected signal by the meanders in the south part. The potential role of the spatial variability of the jet on IT, which includes the meanders, has also been suggested in **?** by studying the reflections by the Gulf Stream.

To conclude about this investigation, the method extracts from the data an energetic incoherent wave of the form of a stationary wave, composed by deflections by the meanders. This wave accounts represents between $40-50\%$ of the incoherent energy for W1-W4and one third , and 30% for W5 (see Fig. **??**), and is the result of a triadic interaction between the coherent wave and the meanders. Even though the incoherent wave is not particularly weak, we find that, in the present configuration, single scattering interactions are still dominating the incoherent propagation of the **??**(**c**)).

In conclusion, we have shown that the proposed statistical methods – BBPOD and EPOD – allow to extract and interpret a wave through a jet with limited spatial extent. Furthermore, the correlation between the most energetic incoherence and the dominant structures of the balanced motion motivates the development of estimates for the full dynamics, with such modal decomposition, in case of entangled observations. This is shown in field scattered by mesoscale turbulence, and in particular to quantify the energetic contribution of the dominant modes of variability of the wave field in connection with the next section.

variability of the mesoscale flow. The EPOD shows that the meanders of the mesoscale jet generate an incoherent wave in the form of a standing wave, made up of deviations in directions determined by the primary interactions.

4.3 Estimation

~~The estimation technique (??) is performed for the reference simulation~~ The second part of this study is dedicated to the problem of estimation, implementing the algorithm **??** introduced in the previous section. Most of the results are shown for the W1 ~~. We start in this study by analysing the capability of the technique to disentangle the two dynamics from a single observation. Then, we evaluate the sensitivity of the estimates to a spatial deterioration of the observations. In practice, we separate the time series into a training and a testing dataset. The POD and EPOD modes are computed from the former, which has an approximate duration of 1300 wave periods (16 months of simulation). The dataset for testing contains 50 snapshots of the complex amplitudes separated from 4 periods, so that the full time series contains 200 wave periods.~~reference simulation. The time series are divided into a learning window and a test window which duration (for the W1 run) is $\approx$ 1300 wave periods – 16 months – and $\approx$ 200 wave periods (50 snapshots separated by 4 wave periods), respectively. For the sake of simplicity, the estimate of the wave is based on the estimate of its complex amplitude, as the total wave can be reconstructed without loosing accuracy (using Eq. **??**).

4.3.1 Estimation ~~for~~ from a full SSH observation

Figure **??** shows ~~estimates~~ an estimate of the SSH ~~contribution of IGW and the jet, from an observation of the total SSH~~ , component of the wave and mesoscale fields, calculated from a complete SSH observation using 30 POD/EPOD modes. ~~It indicates an accurate estimate of the two dynamics, where the dominant patterns are recovered, with a small point-by-point error. For both, the error shows a disorganised field with no evidence of a well identified structure, which would not be captured by the method. To compare with a naive method, another estimate of the wave is shown in appendix. **??** (Fig. **??**) computed with the optimal bases for the two dynamics (POD for the jet and BBPOD for the wave). While being optimal, the BBPOD basis cannot estimate the wave component at all, and requires a more sophisticated algorithm at least. It highlights therefore the interest of the EPOD method in this configuration, for a simultaneous estimation of the jet and the wave.~~ Qualitatively, the estimation is in good agrement with the reference, and the error does not exhibit any particular structure or bias.

~~In Fig. **??** is plotted the mean energy captured by an estimate of the wave taking 30 modes, at each point of the domain. The graph shows a quite accurate estimate of all the wave components, with more than 50% of the energy recovered at approximately each point of the domain. It thus shows a simple data-driven alternative to recover the velocities component without the knowledge of the polarisation relation of the wave field. It suggests also that the estimated snapshot of Fig. **??** is representative of the ability of the algorithm to disentangle the low and high frequency dynamics from the dataset of test. Normalized mean energy reduction of the wave field $(\tilde{u}_\omega, \tilde{v}_\omega, \tilde{h}_\omega)$: $1 - \mathbb{E}\left[|\hat{\boldsymbol{q}}_\omega - \boldsymbol{q}_\omega|^2\right] / \mathbb{E}\left[|\boldsymbol{q}_\omega^2|\right]$, for an estimate over 30 modes, for W1.~~

~~Lastly, in Fig.**??** is quantified~~ The accuracy of the ~~performance of the proposed method by computing the time-averaged~~ estimate (with respect to the number of modes considered) is quantified via the L^2 norm ~~error for the state vector $(h, u, v)^T$~~

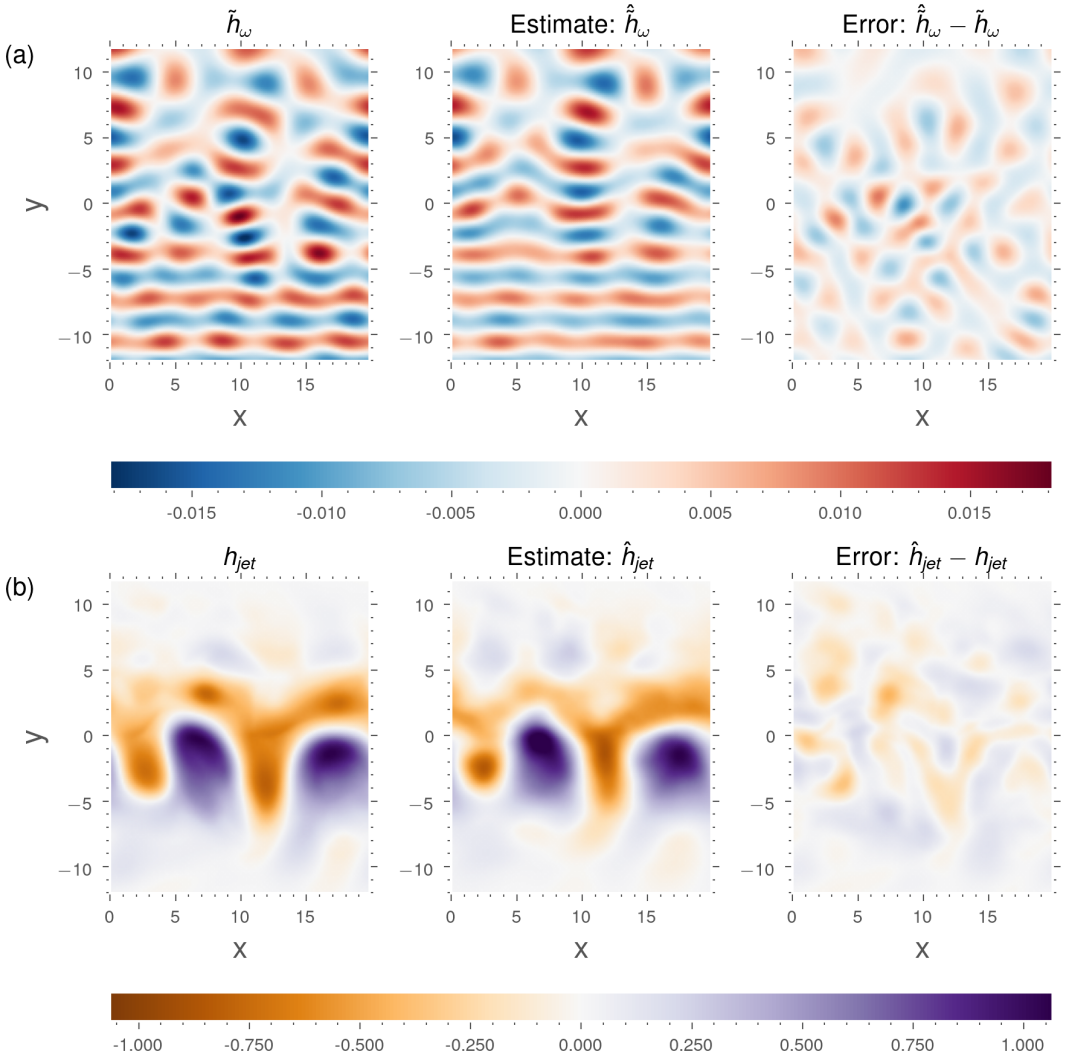

Figure 6. Estimate of the SSH contribution of the wave (**a**) and of the jet (**b**) for 30 modes from one snapshot, for W1.

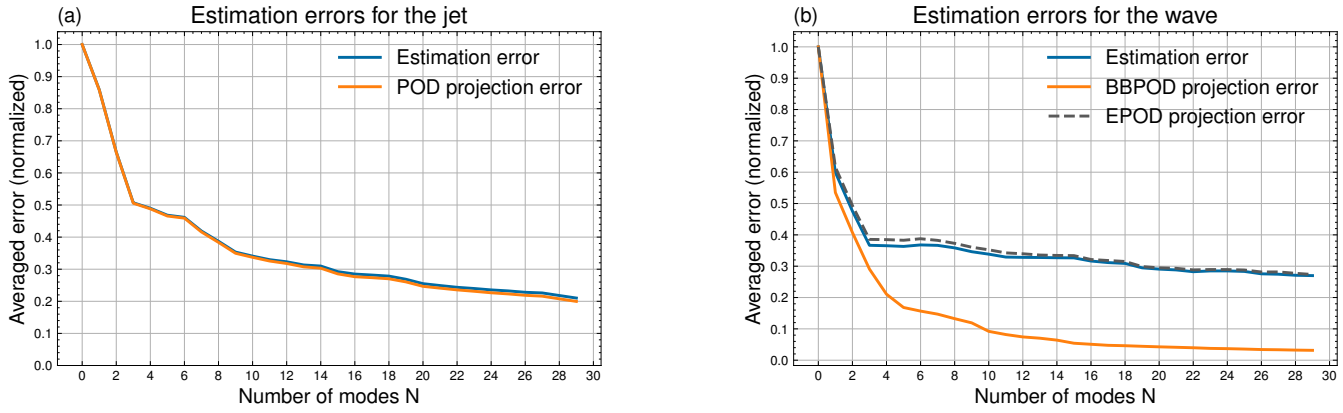

Figure 7. Time-averaged L^2 norm errors (blue) as a function of mode numbers included, together with the projection error of the corresponding POD decompositions, for the turbulent jet (**a**) and the wave field (**b**). For the wave, the EPOD decomposition Eq.(**??**) is also plotted (orange). The results correspond to the W1 run.

~~associated with each type of motion, *i.e.* $\mathbb{E}\left[\|\hat{\tilde{\boldsymbol{q}}}_\omega - \tilde{\boldsymbol{q}}_\omega\|^2_{L^2}\right]/\mathbb{E}\left[\|\tilde{\boldsymbol{q}}_\omega\|^2_{L^2}\right]$ for the wave field and $\mathbb{E}\left[\|\hat{\boldsymbol{q}}_{jet} - \boldsymbol{q}_{jet}\|^2_{L^2}\right]/\mathbb{E}\left[\|\boldsymbol{q}_{jet}\|^2_{L^2}\right]$ for the low-frequency motion. The estimate errors are~~ of the error, averaged over the entire test window, for the complex wave amplitude: $\mathbb{E}\left[\|\hat{\tilde{\boldsymbol{q}}}_\omega - \tilde{\boldsymbol{q}}_\omega\|^2_{L^2}\right]/\mathbb{E}\left[\|\tilde{\boldsymbol{q}}_\omega\|^2_{L^2}\right]$, and for the mesoscale part: $\mathbb{E}\left[\|\hat{\boldsymbol{q}}_{jet} - \boldsymbol{q}_{jet}\|^2_{L^2}\right]/\mathbb{E}\left[\|\boldsymbol{q}_{jet}\|^2_{L^2}\right]$ (Figure **??**). The estimation error is compared with the averaged projection error performed when the ~~fields are projected on their respective POD basis (POD for the jet and BBPOD for the wave). Thus, for the wave the BBPOD projection corresponds to the projection of the wave onto its BBPOD modes following Eq. . By optimality of BBPOD and POD, the latter decompositions minimise the residual variance, hence it provides a lower~~ jet is projected on its POD basis and the wave on its BBPOD basis. Indeed, the projection error measures the ability of the basis learned from the training window to span the observations from the test window: it indicates the maximum energy that can be captured by N modes (this is an inherent property of the POD) and thereby provides a minimal bound for the ~~error associated with the estimate.The figure indicates that the algorithm estimates properly all components of the jet field vector, while only h is observed~~estimation error. Also shown is the EPOD projection error, which corresponds to the error between the true complex amplitude field and a decomposition over N extended modes, wherein the coefficients are calculated by projection of the jet on its POD basis.

We see in Fig. **??** that the estimation error decreases over the first 30 modes for each of the fields. Using 30 modes, 80% of the mesoscale energy is captured. For the wave ~~part, more than 70%~~ (Fig. **??a**), the estimate captures around 73% of the total energy and 63% of the incoherent energy ~~is recovered. Both errors decrease with the number of modes up to 30 modes, suggesting that a large number of modes can be taken for performing estimates. A slope break is visible in~~ (associated with the norm defined in equation (**??**)). The total coherent energy of the test window corresponds to the energy captured by the projection of the wavefield onto the first BBPOD mode, which is 54%. The total incoherent energy corresponds to the residual, and the incoherent estimate corresponds to the estimate of the ~~errors at the third mode , which corresponds to the dominance of the meanders~~ sub-optimal EPOD modes. The error reduction decreases as the number of modes increases, wich is very fast u

Furthermore, we observe that the two error estimates (for the mesoscale and the wave) have a similar shape, with a clear break in slope from the 3rd mode – mode 2 and 3 corresponding to the meandering of the jet and the associated ~~wave response , as discussed in~~ response in the form of a standing wave for the wave (*c.f.* Sect. **??**~~. The energy distribution of higher modes is more homogeneous leading to a slower decreasing error. Note that there is a small amount of energy that is lost for the coherent part (see estimate at mode 1 in~~), which reflects that the dynamics of both motions is coupled.

For the mesoscale (Fig. **??**~~) between the estimate and the BBPOD projection. The EPOD projection error, which corresponds to the decomposition of the wave that is correlated to a N-th order decomposition of the jet is computed by projecting the jet onto its POD coefficients (following Eq.), is also shown in the figure (panel **a**). The small gap between the EPOD projection error and the estimate error (which turns out to be smaller) shows that this simple algorithm can accurately estimate the part of the wave that is correlated to~~ **a**), since the POD basis is optimal and the SSH field is mainly dominated by the ~~jet. Indeed, this stems from~~ turbulent jet, the estimation and projection errors collapse. This suggests that the jet coefficients – including for the velocity component, which are included in the error norm – are perfectly estimated. This shows that the SSH is sufficient to estimate the jet flow, which is consistent with the fact that the jet ~~coefficients are optimally recovered as stated before (see~~ is almost in geostrophic balance. For the wave estimate (Fig. **??b**)~~. Finally, the gap between the estimate~~ , one sees a difference between the estimation error and the BBPOD projection error~~associated with the wave field for a large number of modes shows some limitation of this method. Apart from the missing coherent signal accounting approximately for~~ . Already for the first mode (corresponding to the coherent part), there is approximately 8% of the total ~~signal, thiscan be explained firstlyby the fact that only~~ energy that is missing in the estimate. There are several possible explanations for this: firstly, the wave estimate only contains the part that is correlated with the jet and not the part that is decorrelated. Also missing is the ~~part of the wave correlated to the jet is estimated, as stated in Sect. **??**. Another reason is that the jet is only estimated at 80% (with 30 modes) and therefore, the wave estimate misses the part correlated to the remaining~~ fraction of the wave field correlated with the residual of the jet estimate over the 30 POD modes (which represents 20% of the jet~~. For a turbulent jetthat can be expressed by fewer modes, that is said "low-rank", the algorithm is expected to perform slightly better at least. In appendix. **??** is shown in Table **??**~~'s energy). Secondly, non-stationarity effects in the flow can partially degrade the estimation of correlations between the wave and the jet. Despite the limitations that have been mentioned, we see that for a total observation of SSH, one can have confidence in a large number of modes to estimate the wave and jet fields.

The wave estimation error presented above is calculated for every simulations W1–W5 in table **??**. The numbers shown correspond to the minimum of the ~~maximal values of averaged energy captured on the first 30 modes , for the simulations W1-W5, as it shown in Fig. **??**. This highlights that apart from the small scale wave simulation,~~ error as a function of the number of modes for the ~~algorithm can estimate~~ first 30 modes (corresponding to the maximum energy captured). With the exception of the W2 simulation, which represents a wave of higher frequency compared to the other runs, the method captures more than 73% of the total wave ~~field~~energy for each of the simulations, and between ~~44% — 63%~~ 44 and 63% of the incoherent ~~part, even for the strong mesoscale flow associated with an energetic incoherent wave (Fig. **??**). While reducing some of the variance of the incoherent part, the algorithm performs worse for the run~~ energy. Moreover, the wave estimate does not diverge as the number of modes increases for these simulations. However, the method seems less effective at capturing a higher

	W1	W2	W3	W4	W5
Total wave field	73%	64%	82%	88%	75%
Incoherent part	63%	21%	44%	63%	50%
Jet	79%	73%	83%	88%	82%

Table 2. ~~Time-averaged L^2 norm errors (blue) as a function of mode numbers included, together with~~ Best mean wave energy captured over the ~~projection error of the corresponding POD decompositions~~first 30 modes, ~~for~~ by estimating the wave~~field (**a**) and the turbulent jet (**b**),~~ for each W1-5 simulation. For ~~the wave~~W1, ~~the EPOD decomposition Eq.is~~ this value can also ~~plotted (orange)~~be seen in Fig.~~It~~ **??**, which is ~~performed for the W1 run~~reached considering the 30 first modes.

frequency wave by correlation in the W2 ~~($\omega = 3f_0$), associated to the fast wave, and starts increasing from the 15 modes (not shown). Yet, this frequency is superior to the M_4 frequency component, which is rather small in practice.~~ simulation. The best estimate is reached in the 12th mode, and diverges very slightly.Unfortunately, we do not have a clear explanation for this. We can simply point out that at high frequencies ($\omega = 3f_0$ being greater than $M_4 \approx 2.8f_0$ at mid-latitudes), the scattering of waves is more complex and more intense (**?**). The estimate of the jet remains fairly robust, since its amplitude remains high for all the simulations. We can also confirm that, by construction of the method, the better the estimate of the jet, the better the estimate of the total wave.

4.3.2 Impact of a partial observation

~~For the last~~ In the final part of the study, we ~~intend to~~ evaluate the sensitivity of the ~~estimation algorithm to a degradation of the spatial sampling. The sparse observationgenerated consists~~ method to the spatial coverage of observations. Figure **??** shows an example of a subsampled observation, consisting of 4 ~~vertical bands of SSH with a typical width of one Rossby radius (see Fig. **??**) and homogeneously distributed~~ SSH vertical bands which are approximatively homogeneously spaced in the domain ~~. Combined with the fact that we do not have information in time, estimating and disentangling the two dynamics is a challenging task.~~ and one Rossby radius wide.

Figure **??** shows ~~a snapshot of the estimated wave and jet fields, computed with 12 modes. The wave estimate exhibits a smoother field compared the the full observation case, as only 12 modes were taken to produce the estimate. The large scale dominant pattern are yet still captured, indicated by a smallerror in all the domain. The estimate for the jetcaptures the global shape, even if there is a more pronounced error compared to the full observation case~~ an estimate over 12 EPOD/POD modes, from the same snapshot as in the full observation case, of the complex amplitude of the wave and the jet. Since fewer modes have been taken into account for the estimation, the wave field is smoother, but the error is still qualitatively quite small.

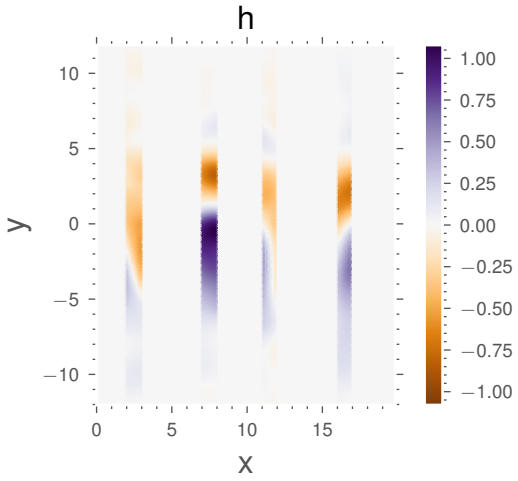

Figure 8. Sparse SSH snapshot observation from the W1 run, covering 20% of the full domain.

For the jet, ~~with some overestimated amplitudes~~the error is more pronounced with higher amplitudes than in the case of total observation. The choice of 12 modes corresponds approximately to the minimum error, as shown below.

715 ~~In~~ We calculate Fig. **??** ~~is shown the time-averaged~~ the jet and wave estimation errors in L^2 ~~norms errors for different spatial coverage of the domain, ranging from 10% (two bands) to 20% (four bands). The results show that~~ norm averaged temporally over the whole test window. We evaluate the sensitivity of the error by varying the observation coverage from 4 bands (covering 20% of the domain) to 2 bands (10% of the domain). With 4 vertical bands, the algorithm is ~~robust to capture the first three modes of the two dynamics for a 20% coverage,~~ still able to estimate the first 3 modes with little difference compared with 720 total observation. These modes correspond to larger jet structures, and therefore seem to be less affected by the degradation of the spatial sampling. From 3 modes, the estimate reaches a plateau for the wave and decreases slightly for the jet. At best, around 60% of the jet's energy is captured and around 65% for the wave. For 3 vertical bands, the error deteriorates slightly but the curves remain similar to the previous case. Finally, the case of 2 bands is more pathological and shows that when the observation space is too small, and the number of parameters to be minimised is too large (here > 11 modes), the error 725 increases. In addition, as in the case of total observations, we note that the coupling of the projection coefficients between the jet and the ~~error still decrease until 12 modes approximately. However, at 15% coverage and below, the convergence of the error is lost. In particular, we find that for very sparse observation coverage (10% of the domain) both estimates are diverging. In this case, the jet is not well estimated and , consequently, the wave cannot be accurately estimated only by correlation. A proper~~ wave means that the error curves for the jet and the wave necessarily follow a similar trajectory, suggesting that a 730 good estimate of the ~~balanced motion is central to accurately predict the wave, and this test case illustrates one limitation of our algorithm. It can be noticed as well that high-order mode's estimation is more sensitive to this progressive observation degradation, suggesting that these high-order modes are more difficult~~ jet is required in order to have a good estimate of the

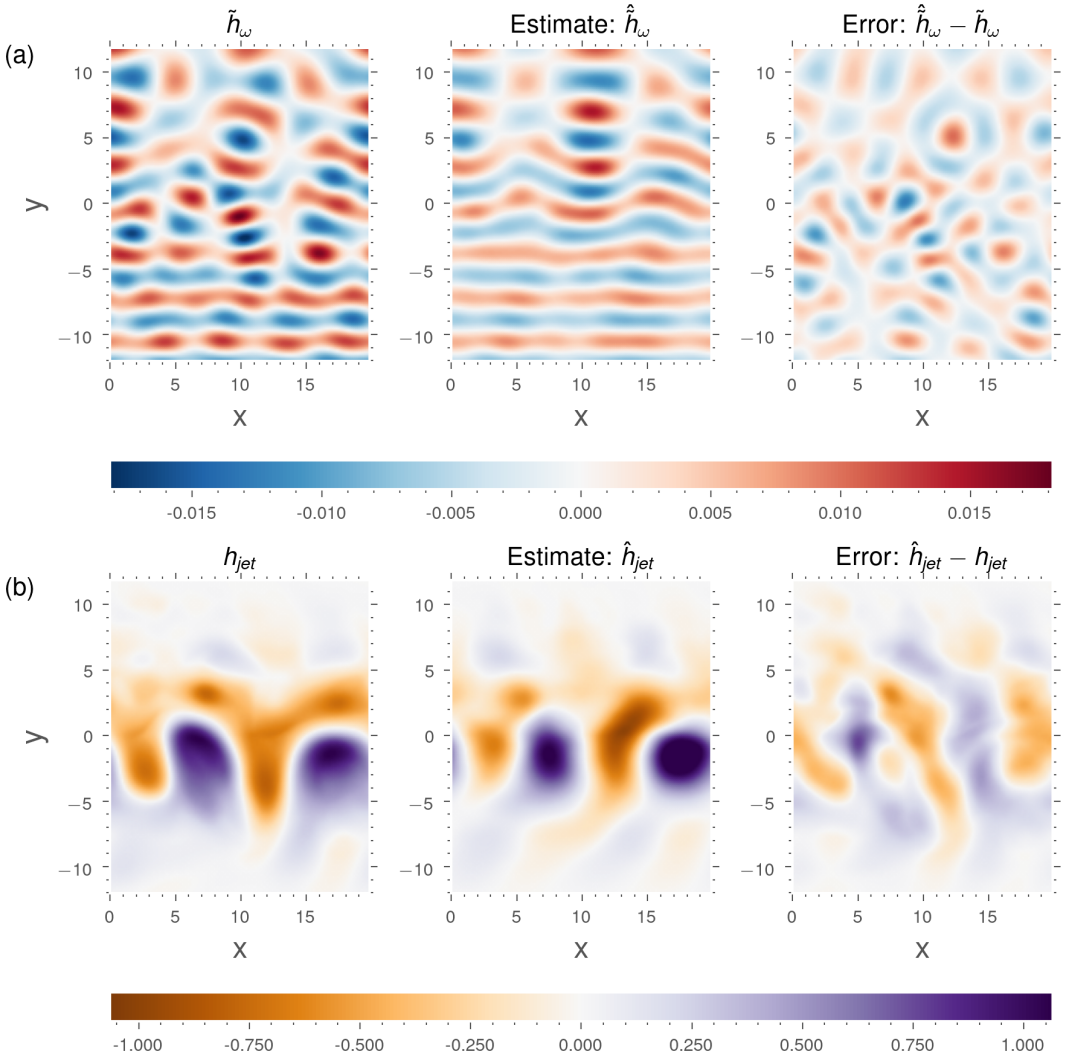

Figure 9. Estimate of the SSH contribution of the wave (**a**) and of the jet (**b**) for 12 modes from one sparse snapshot.

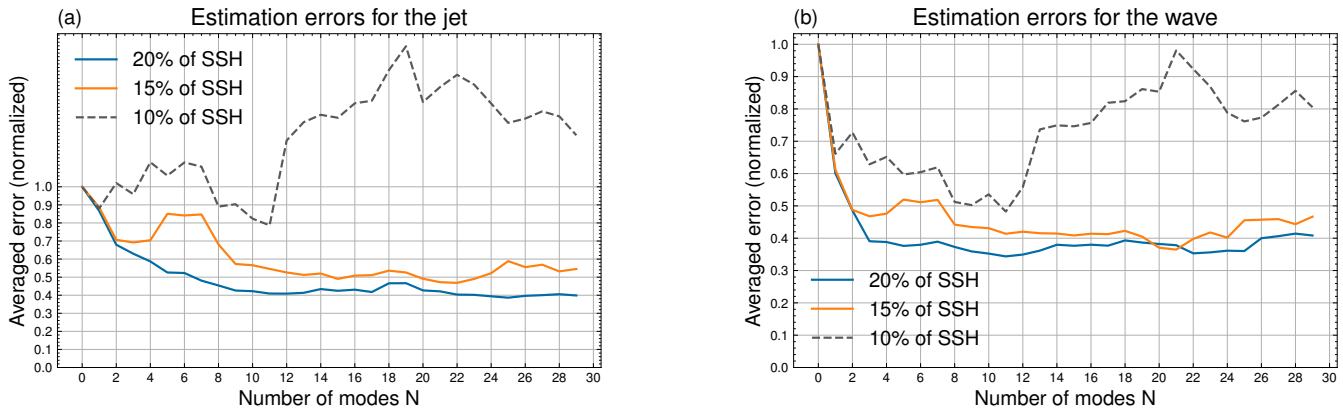

Figure 10. Averaged L^2 norm errors for the ~~wave~~ jet (**a**) and the ~~jet~~ wave (**b**) for sparse observations.

wave. The increase of the error could be mitigated by adding regularising terms to the algorithm, *e.g.* penalizing the amplitude of high modes.

4.4 Discussion

The EPOD-based estimation method presented above relies on the correlation between the mesoscale fluctuations and the scattered wave field to estimate the latter in a regime where the SSH is dominated by the mesoscale, which is probably the main advantage of the method. To emphasise this, an attempt is made to estimate and ~~could lead more likely to a loss of robustness than a gain in accuracy.~~ separate the mesoscale and wave dynamics from single SSH snapshots using a simpler approach, which is detailed in Appendix **??**. This involves considering BBPOD modes (with a specific set of projection coefficients to be determined by optimisation) instead of EPOD modes to express the wave. This approach fails completely in reconstructing the wave field (Fig. **??**). Although making these two bases independent could provide a better projection space (which here is optimal in terms of energy content), the estimation fails because *i)* it subjects the minimisation problem subject to overfitting, *ii)* it discards the statistical links between the two bases supported by their dynamical relation equation (**??**) and *iii)* the wave is poorly observed due to a large relative amplitude difference between the SSH contribution of the jet and the wave. Thus, this comparison highlights the benefit of explicitly accounting for the coupling between the mesoscale and the wave via extended modes.

~~Mitigation of this issue could be achieved by adding a term of regularisation in the algorithm.For one reason, the POD basis ensures that the time-average energy captured per mode (and hence, the coefficient of projection) decrease with mode number, and we did not leveraged this property when minimising the cost function. Regularisation was not used in the present work, because our focus is on describing a new estimation algorithm and showing its performances "as is", without further fine tuning. Nonetheless, it clearly appears that , in the last series of tests above, the optimisation problem becomes ill constrained, since the error diverges (typical of over-fitting regimes) as we increase the number of parameters and /or use sparser observations~~

. Let us know discuss the limitations of the proposed approach. First, the EPOD decomposition of the wave only provides an estimate of the part of the wave that correlates with a truncated POD decomposition of the jet. As discussed above, this contribution is a priori important for an incoherent wave resulting from interaction with a turbulent flow, and if the number of modes included in the decomposition is sufficiently large. Secondly, the decomposition bases should be able to span future observations that have not been learned from the data set. Some of the errors may therefore be due to errors in projecting the wave and jet observations onto their respective bases.

Finally, it can be expected that this approach would become inefficient in configurations where the signature of the IT becomes dominant, and in particular in regimes with very weak mesoscale flows, as the correlation between the mesoscale fluctuations and the wave field would be less pronounced. In this case, recourse to a BBPOD-based algorithm seems more appropriate, provided some improvements are achieved, such as the use of regularisation techniques in the minimisation algorithm to avoid overfitting. For example, **?** showed that a SPOD basis can be used to estimate part of the incoherent signal off the Amazon, using multiple snapshots. Their algorithm estimates the sea surface height (SSH) contribution of the internal tide by finding the IT projection coefficients that minimise the error with multiple observations.

Constructing an algorithm that takes advantage of each method depending on the dynamical regime is a straightforward development that is left for future work. In any case, more sophisticated minimisation algorithms that better constrain the temporal coefficients need to be implemented in order to maintain accuracy as observations degrade. This may include a regularisation term, *e.g.* that penalises higher modes amplitudes, depending on the choice of an appropriate norm and an initial guess on the solution. In a sense, the methods proposed by **?** or **?** are examples of constraints put on the temporal coefficient, by using a harmonic function to link observations at different times.

5 Conclusions and perspectives

In this study, ~~a~~ we have proposed new data-driven ~~method is presented for the study of a~~ statistical decompositions of a (internal) wave scattered by ~~a turbulent flow from numerical simulations. The approach we propose is to study the variability of the incoherent wave, resulting from quadratic interactions of these two motions, through the correlations between the slow wave modulation amplitudes and the jet components, both evolving at similar time scales. To perform this investigation, two decompositions for the wave were used: the EPOD method to extract wave structures correlated to the jetcomponents, and the BBPOD technique capturing optimal modes of the broadband wave field. An explicit theoretical link between the EPOD modes of the wave and the POD modes of the jet is detailed when there is negligible multiple scattering interactions. For an~~ mesoscale turbulence. These decompositions are derived from the POD and describe the slow evolution of the complex amplitude of the wave, driven by non-linear interactions with the mesoscale flow. We first introduced the Broadband POD, which adapts the POD for a scattered wavefield with a broadband spectrum. Then, we proposed a decomposition of the wave field that extracts its fraction correlated with the jet, using the Extended POD (EPOD) method – which is probably the most important aspect of this study. We have highlighted a dynamic link that exists between the extended wave modes and the mesoscale POD modes,

which holds under certain wave scattering regimes (dominant and localised primary interactions), and allows for a physical interpretation of the extended modes.

We have demonstrated, using idealised rotating shallow water ~~configuration where a wave is propagating through~~ simulations, the ability of both decompositions to analyse the scattering of a low-amplitude wave by a zonal jet~~, the numerical results confirm this connection. It has been demonstrated that for different waves and different jets~~. For different wave and mesoscale fields, the dominant ~~modes of IGW are directly driven by those of the jet, resulting from single-scattering interactions with the coherent wave. It has been shown that a large fraction of the energy of the~~ BBPOD modes of the wave results from the interactions between the dominant mesoscale POD modes and the coherent part of the wave. A significant part of the incoherent wave is a standing wave ~~resulting from the deflection of the coherent wave~~ generated by the meanders ~~, according to this single interactions.~~ of the jet, determined by these primary interactions.

~~Based on this method, we derived a simple data assimilation scheme to demonstrate the capacity of such decompositions to produce a simultaneous estimation of the jet and the wave~~ In the second part of this study, we addressed the issue of disentanglement of wave and mesoscale flow from a single ~~entangled observation of SSH . The EPOD method is here meant to capture the IGW signal by correlation to the jet. In the case of a turbulent balanced flow dominating the SSH signature, the EPOD method reveals its interest in order to estimate the weak IGW signal. Using only a single snapshot of fully-observed SSH, the algorithm is able to estimate accurately all the components of the jet and the wave. The low-frequency dynamics is optimally estimated (by property of the POD basis), and for the wave most of the wave patterns were captured, accounting for approximately more than 70% of the total energy. However, the case of very incomplete observation shows that high-order modes should be discarded and highlights the limitation of this simple assimilation scheme. As there is a coupling with the jet components through the method, a proper estimate of the low-frequency dynamics is required to estimate the IGW signal. To address this issue, appropriate regularisation terms could be added on this algorithm to better assimilate higher modes. There is also a need to better quantify the part of the wave that is decorrelated from the jet~~SSH snapshot. Our method relies on a simple minimization algorithm wherein the SSH observation is expressed as the sum of a mesoscale contribution, decomposed on a POD basis, and wave contribution correlated with the jet, decomposed on the Extended POD modes. This coupled POD/EPOD estimation algorithm makes it possible to estimate a wave field of very weak amplitude (notably compared with the mesoscale contribution) from isolated snapshots of SSH, including the velocity field, and allows to estimate the incoherent wave field (we captured between 44% and 63% of the incoherent wave energy in the idealised RSW simulations), which can potentially give us access to derived quantities such as incoherent wave energy fluxes.

Although this study was primarily motivated by the issue of estimating internal tides, the EPOD method has a fairly general formalism and could be applied to different types of scattering, as long as the scattered wave essentially arises from a interactions between well-identified incoming wave on the one hand, and time-varying flow on the other hand. This includes, for example, scattering of near-inertial waves in the ocean, the loss of coherence of barotropic tide in coastal areas, or the scattering of acoustic waves by turbulence. Also, this method could be applied to waves of large amplitude, since they remain correlated with the turbulent flow, which is ~~missing in the algorithm.~~ a straightforward extension of this study. Finally, three-dimensional

scattering can be studied (**?**), for example by considering global three-dimensional EPOD modes, or by combining with other decompositions such as the vertical mode decomposition for IT.

~~Even though the method is for the moment limited to theoretical and idealised configuration, this provides some interesting motivations for adapting it~~ Another important perspective of this study is to adapt these methods to more realistic cases. ~~Indeed, the long revisit time of altimeters poses a problem to disentangle the two dynamics from observations. Thus, the ability of the algorithm to produce accurate estimates from single snapshot is a property that could be beneficial for such difficult configurations. Furthermore, as the method is meant to estimate IT in region with strong mesoscale flows, it could also help addressing the issue of the disentanglement of the two dynamics in these particular region, as in the Gulf Stream for instance. **?** also demonstrated that similar data-driven and modal decomposition technique could be envisaged to estimate IT from real observations. Yet, more work is required to test the ability of the present modal decompositions to capture the two dynamics in realistic configurations . The method is firstly envisaged to be adapted on larger domains, by incorporating localisation technique, which is the object of an ongoing study~~A few limitations need to be addressed in order to achieve this. First, the use of instantaneous correlation between the jet and the wave is mainly valid for estimating the wave locally. It is also necessary to improve the convergence of statistical estimates so that the decompositions that are proposed can cover a high-dimensional space. This would improve the estimation of observations that have been insufficiently learned from a reduced-size time series and that are not represented in POD/EPOD modes. It also makes it possible to extend the estimation of waves and currents to the scale of an ocean. Localisation techniques, which broadly consist of defining localised sub-domains to enable considering localised interactions and artificially increasing the number of samples, could address these issues (**??**). Another methodological challenge to address more realistic configurations is that the internal tide field contains several nearby frequencies. How to separate each coherent peak in the data and adequately describe their correlation with the turbulent flow remains to be understood. Therefore, we think that further work on idealized cases are required before applying this method to a realistic case.

Code and data availability. The subsampled time series of lowpassed filter and complex demodulated output of the RSW simulation W1 are provided at https://gitlab.inria.fr/imaingon/internal-tide-simulation.git, including codes to produce data and diagnostics.

Appendix A: Equivalence between Broadband POD and SPOD

This appendix presents the algorithmic specifities of the common SPOD algorithm using the Welch method (**?**) to estimate the CSD, and its relation to the BBPOD algorithm, that is used in this study. For some well chosen parameters, we show that the two algorithms are equivalent.

The following proof is performed with discrete variables, considering a signal x_t with time spacing Δt and $t_k = k\Delta t$.

Proof. The complex demodulation writes:

$$< x_t e^{-i\omega t} >_j = \sum_{k=-m}^{m} b_k x_{j-k} e^{-i\omega t_{j-k}}$$
$$= \sum_{k=j-m}^{j+m} b_{j-k} x_k e^{-i\omega t_k}, \tag{A1}$$

where $(b_i)_{-m\leq i\leq m}$ are the discrete coefficients of the filter $< \cdot >$.

Besides, the principle of the Welch method is to subdivise x_t into possibly overlapping blocks of size ~~N~~ N with an overlap N_o. A Fast Fourier Transform is then performed on each windowed block to extract the Fourier component at the tidal frequency, denoted X_ω^l where l is the block index. So,

$$X_\omega^l = \sum_{k=-N/2}^{N/2} x_{k+l(N-N_o)} W_k e^{-i\omega t_k}, \tag{A2}$$

where W_k is a window function defined on $[-N/2, N/2]$.

By changing variable $k' = k + l(N - N_o)$, it follows

$$X_\omega^l = e^{i\omega t_{l(N-N_o)}} \sum_{k'=l(N-N_o)-N/2}^{l(N-N_o)+N/2} x_{k'} W_{k'-l(N-N_o)} e^{-i\omega t_{k'}}. \tag{A3}$$

Assuming that the window function is symmetric in the middle of each block (which is verified for most windows used in the literature), ~~i.e~~ *i.e.* $W_k = W_{-k}$, ~~Eq.~~Eq. (**??**) gives

$$X_\omega^l = e^{i\omega t_{l(N-N_o)}} \sum_{k'=l(N-N_o)-N/2}^{l(N-N_o)+N/2} W_{l(N-N_o)-k'} x_{k'} e^{-i\omega t_{k'}}. \tag{A4}$$

Finally, by choosing the window function as the filter coefficients, *i.e.* $W_k = b_k$ and $m = \frac{N}{2}$, relation Eq. (**??**) yields:

$$X_\omega^l = e^{i\omega t_{l(N-N_o)}} < x_t e^{-i\omega t} >_{l(N-N_o)}. \tag{A5}$$

Consequently, up to a phase, the FFT of a block l of size N with overlap N_o at ω corresponds to the complex demodulation of the signal at time $l(N - N_o)$. The phase shift cancels when computing the correlation over N_b blocks:

$$\sum_{l=0}^{N_b} X_\omega^l {X_\omega^l}^* = \sum_{l=0}^{N_b} < x_t e^{-i\omega t} >_{l(N-N_o)} < x_t e^{-i\omega t} >^*_{l(N-N_o)}. \tag{A6}$$

Therefore the Welch method computed with parameters (N, N_o, N_b, W) is equivalent as to compute the complex demodulation of the time series over N_b snapshots sampled every $N - N_0$ and a filter chosen as the common window function W (Hann, Hanning~~...~~, ...). □

This simple proof highlights the fact that the window function in the Welch method is playing the role of the filter in the BBPOD method. ~~An advantage of the BBPOD algorithm for our study is that the frequency band covered by the window~~

function is made explicit in order to extract the broadband wave field. In SPOD the paradigm is more to efficiently capture each harmonic separately, and to compute a basis at each frequencyin the wave spectrum to capture all effects of incoherences. Using SPOD for spectral broadening problems would suggest to collect SPOD modes at neighbour frequencies an resort them in terms of energy content (as in **?**). It would raise the issues of loss of orthogonality of the mode's family with respect to the spatial innerproduct, and to interpret properly the modes taking into account the potential spectral overlap induced by the Welch window, or at least to design it for purpose. We believe than that it makes it less adapted for studying broabdand fields as compared to the BBPOD method. Although the two methods are equivalent, they differ in their use and interpretation, and also in the choice of parameters. BBPOD is designed to extract a broadband signal, the width of which is chosen via a filter using physical time scales. SPOD looks for an orthonormal basis for the Fourier coefficients at a given frequency, and the parameters of Welch's algorithm are chosen to minimise spectral leakage for a given amount of data. Techniques for reconstructing a broadband spectrum using several SPODs at each frequency of the spectrum are possible by reordering their energy contribution (Nekkanti and Schmidt 2021). On the other hand, the orthogonality property of the modes is lost, since the SPOD modes are no longer orthogonal at different frequencies.

In the following is presented some complementary figures for the estimate part of Sect.**??**. First of all, a

Appendix B: Wave estimation using BBPOD instead of EPOD

A test has been performed in order to show the importance of informing the correlation between the jet contribution and the wave through EPOD in the estimation problem. A similar estimation than in Fig. **??** is performed, but independent coefficients a_k and b_k are sought for the estimation, instead being connected through EPOD. Results are shown in Here, a "naive" algorithm is implemented, wherein the wave on its optimal basis BBPOD (instead of EPOD) and the jet on its POD basis. Instead of considering the same coefficient $a_n(t)$ for the jet POD mode and the wave EPOD mode, two independent sets of coefficie which is given by:

$$\min_{(a_n,b_n)} \| \sum_{n=0}^{30} a_n \psi_n(\boldsymbol{q}_{jet})_h + \Re[b_n(\psi_{n,\omega})_h e^{i\omega t}] - h\|^2.$$

As visible in Figure **??**, to be compared with Fig. **??**, and estimation errors are very large. Obviously, the optimal coefficients should lead to a lower error since some constraints are relaxed, but finding them becomes a hard task without physical information (provided by EPOD in our method), or advanced regularisation in the optimisation problem. **??**, the corresponding estimate is completely wrong. Possible reasons of this falure are provided in the body text.

Secondly, estimates errors given a full observation are computed for the five simulations that are presented in Sect. **??**, following algorithm **??**.The maximal variance captured by

Appendix C: Effect of Rossby number on the modal decompositions

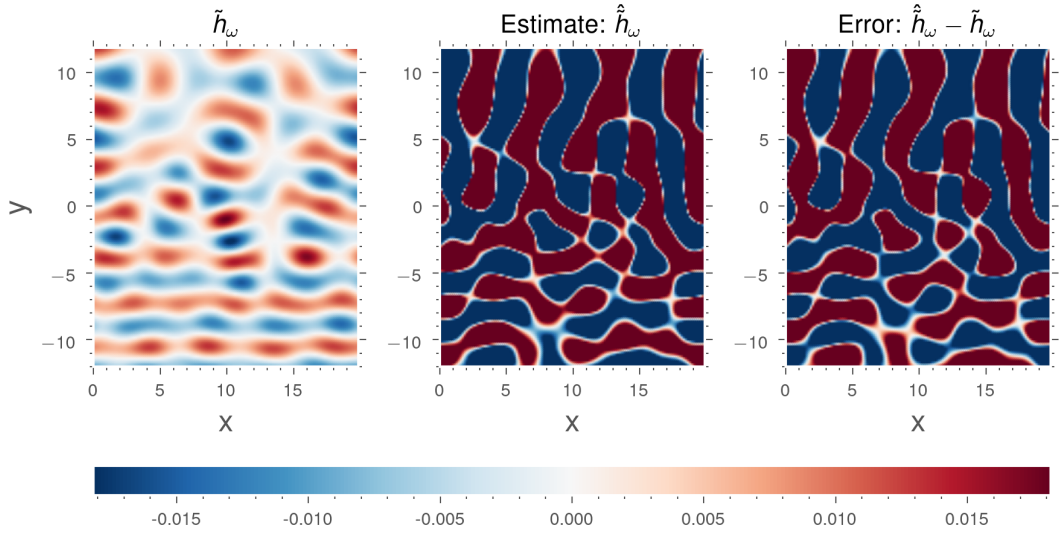

Figure B1. Estimation of the SSH contribution of the wave for the W1 run, computed from one snapshot, using 30 modes of the optimal basis of the jet and the wave vectors (POD for the jet, BBPOD for the wave). ~~The BBPOD coefficients b_n to recover the wave are computed according to the minimisation problem: $min_{(a_n,b_n)} \| \sum_{n=0}^{30} a_n \psi_n(\boldsymbol{q}_{jet})_h + \Re[b_n(\psi_{n,\omega})_h e^{i\omega t}] - h \|^2$.~~

In this section we show the POD modes of the jet (Fig. **??a**) and the EPOD modes of the wave (Fig. **??b**) for the W5 simulation. This simulation is characterised by a higher Rossby number. The consequence is a change on the jet dynamics, and then in the scattered wave fields. This effect is visible in the ~~estimated wave field considering the first 30 modes is shown for each run in Table **??**, as well as the fraction of the incoherent component that is recovered.~~ results of the modal decompositions. The jet POD and wave EPOD modes show similar structures to W1-W4, but the wavelengths of modes 1 and 2 are twice as long.

~~Mean-energy reduction W1 W2 W3 W4 W5 Total field 73% 64% 82% 88% 75%Incoherent part 63% 21% 44% 63% 50% Maximal values of variance recovered by the wave estimate for the first 30 modes, for each simulation given complete SSH observations. The values for the W1 run can be found in the corpus on Fig. **??** for 30 modes.~~

Author contributions. IM wrote the article, performed the numerical tests, and were implicated in the methodology of this study. GT and NL both supervised the global validation of the results and reviewed the article. They provided expertise on each section of the paper, and contributed to the formal analysis and to the global methodology of this article.

Competing interests. The authors declare that they have no conflict of interest.

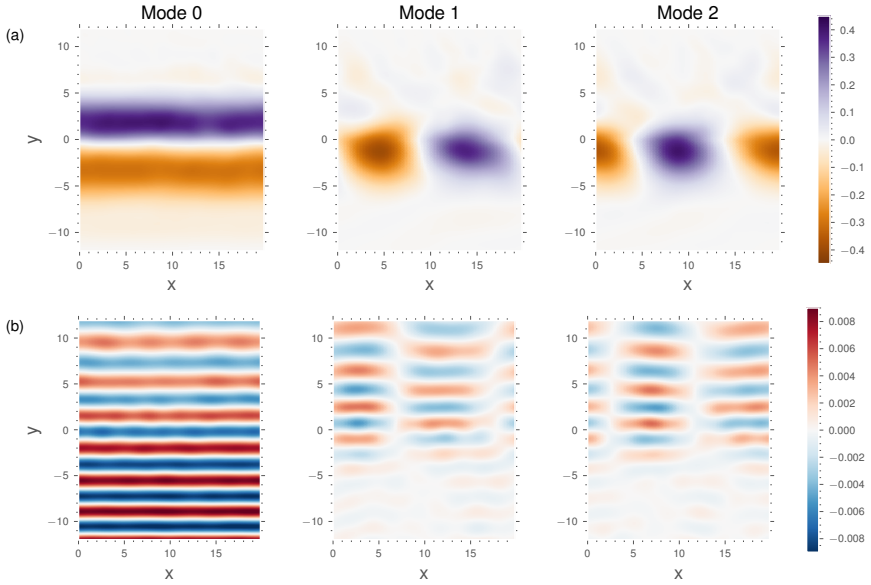

Figure C1. Three leading POD modes of the jet (**a**) and the associated EPOD modes of the wave field (**b**) for simulation W5. They are weighted by the square-root of the respective POD eigenvalue $\sqrt{\lambda_n}$. The first three eigenvalues are $\lambda_0 = 8.86, \lambda_1 = 3.29, \lambda_2 = 3.21$.

Acknowledgements. N. Lahaye had support from the French research funding agency under the ModITO project (ANR-22-CE01-0006-01) and from the TOSCA-ROSES SWOT project DIEGO. G. Tissot and N. Lahaye acknowledge support from the French National program LEFE (Les Enveloppes Fluides et l'Environnement).